Author/s:
Chen Reddy, Sushma Reddy

Title:
Investigation of air-sea fluxes over the Southern Ocean using an eddy-covariance technique and parameterization using stability functions

Date:
2019

Persistent Link:
https://hdl.handle.net/11343/238588

Investigation of air-sea fluxes over the Southern Ocean using an eddy-covariance technique and parameterization using stability functions

Sushma Reddy Chen Reddy

ORCID: 0000-0001-5668-9108

A thesis submitted in total fulfillment for the
degree of Master of Philosophy

School Of Earth Sciences
THE UNIVERSITY OF MELBOURNE

April 2020

Declaration of Authorship

This is to certify that:

- The thesis comprises only my original work towards the Master of Philosophy except where indicated;
- due acknowledgement has been made in the text to all other material used; and
- the thesis is fewer than the maximum word limit in length, exclusive of tables, maps, bibliographies and appendices as approved by the Research Higher Degrees Committee.

Signed: Sushma Reddy Chen Reddy

Date:

Acknowledgements

Firstly, I must acknowledge and thank my supervisors, Dr. Robyn Schofield and Associate Professor Jason Monty, for giving me the chance to pursue research. I want to thank you for the advice and guidance whenever they were needed. I am grateful to have been allowed to work independently, knowing that a helping hand was just around.

I would also like to thank my advisory committee, Prof. Peter Rayner, Dr. Jay Black, Prof. Ian Simonds, and Dr. John Moreau for all their ideas, encouragement, advise, and support throughout the project. Their counsel has had significant influences on the project.

I want to thank Byron Blomquist from NOAA and Brett Muir from CSIRO for providing me with the CAPRICORN data and R/V Investigators attitude and navigation data and for sharing their knowledge on computing the platform motions and their insightful suggestions.

A special mention goes to Dr. Will Lee, Mr. Derek Jacquest, Tunggul Bhirawa, Shuo Lee, for their assistance while working in the Hydrodynamics lab and for their suggestions and discussions. Without their experience and support, it would have been impossible for me to do the experiments. The time I spent in the hydrodynamic laboratory will always remain a good learning experience for me.

Also, I would like to thank Toni Fraser, Charlotte, Karla Fallon, Jan May, and Katrina Sewell for their assistance with many administrative tasks and their kind friendship.

I would like to thank all my friends and colleagues, past and present, Harika Raavi, Robert Ryan, Sonya Fiddes, Karishma Noore, Achyut Mishra, Mahesh Indrajeetsingh, Apoorv Jyothi, Meghalim Phukan and too many others to name, for their support and friendship especially during difficult times and for becoming a family away from home.

I want to thank my parents, Bhagya Lakshmi and Bojji Reddy, who prioritize the education of their children, also to my sister Greeshma Reddy, for supporting me throughout. I appreciate and admire your endless patience, constant support, and encouragement throughout my life. I am forever indebted to you.

Abstract

The Earth is an integrated system that consists of sub-systems that interact and influence each other. These interactions have an important influence on the understanding of weather and climate of the earth system. Air-sea interactions are one such interaction that affects the Earth's system thus making it essential to understand the physical processes that affect the prediction and forecast of the weather and climate. The present state of art climate and numerical weather prediction models use bulk models which are based on Monin-Obukhov similarity theory and Charnock's relations to determine the fluxes across the air-sea interface. The COARE 3.5 model is the best performing model available, and it is seen that the model underestimates the fluxes at higher wind speeds. Hence, to avoid any assumptions and circular dependencies, we need to build a simple parameterization of coefficients of fluxes to determine fluxes.

Eddy Covariance, the purest form of flux calculation, is used to develop the parameterization. Eddy covariance relies on high-frequency 3-D winds, which, on ships, are contaminated by platform motions. However, in the absence of reliable accelerometer data, or a failed collocated accelerometer, calculating these motions is difficult. Here, in this study, we studied if the ship's motion reference data can replace external collocated accelerometer data. We have characterized that for the anemometer mounted on the foremast of the R/V Investigator, and there is a lag of 1.4 sec in the ship's motion reference unit data. Hence, we can correct the wind speeds for platform motions using the ships' motion data after adjusting to the lag. The spectral speak due to the platform motions observed in the measured raw data by anemometer is removed after the corrections performed by the ship's data. Hence, achieving the redundancy of the external collocated accelerometer, GPS receiver, and heading sensors.

The fluxes computed from the eddy covariance technique are used to get a simple parameterization to estimate fluxes. Here, we have developed the coefficients of drag, latent heat fluxes in terms of simple functions of Reynolds and bulk Richardson number, which are physically dependent on velocity and stability of the atmospheric boundary layer. The model proposed does not depend on any assumptions or does not have any circular dependencies. The coefficient of sensible heat flux could not be parameterized as we observed that there is no dependence on Reynolds number in the neutral, stable region. The proposed model is performing better compared to that of the COARE 3.5 model at higher wind speeds.

Gas transfer across the air-sea interface is challenging to measure, and the existing relationships for the gas transfer velocity with wind speeds have a high variance at high wind speeds. It is essential to measure gas transfer velocities in the Southern Ocean as

it is least sampled with the rough environment and high surface waves. It is estimated that the Southern Ocean is the largest sink of anthropogenic carbon dioxide, with about 40% of the total world ocean sink. Gas transfer velocities of CO_2 in the Southern Ocean are measured, and it is found that the results obtained are within the range that is reported by the previous researchers. However, there are no sufficient data points, and the variance in the data is high to get any conclusions from the results obtained.

Contents

List of Figures

List of Tables

Abbreviations

ABL	Atmospheric Boundary Layer
ASL	Atmospheric Surface Layer
CAPRICORN	Clouds, Aerosols, Precipitation, Radiation, and atmospherIc Composition over the southeRn oceaN
CCN	Cloud Condensation Nuclei
COARE	Coupled Ocean - Atmosphere Response Experiment
CRDS	Cavity Ring Down Spectroscopy
DIC	Dissolved Inorganic Carbon
DMS	Dimethylsulfide
EASI	The Extreme Air-Sea Interaction facility
ECMWF IFS	European Centre for Medium-Range Weather Forecasts Integrated Forecast Systems
LHF	Latent Heat Flux
MOST	Monin-Obukhov Similarity Theory
MRU	Motion Reference Unit
NDIR	Non Dispersive Infra-Red
NOAA PSD	National Oceanic and Atmospheric Administration, Physical Sciences Division
NWP	Numerical Weather Prediction
OBL	Oceanic Boundary Layer
RegCM	Regional Climate Model
SHF	Sensible Heat Flux
SO	Southern Ocean
SIWWI	Sea-Ice Wind Wave Interaction facility
TOC	Total Organic Carbon

Symbols

C	Charnock's constant
cg	Centre of gravity
C_a	Concentration of gas in air
C_D	Coefficient of drag
C_E	Coefficient of latent heat flux
C_H	Coefficient of sensible heat flux
C_w	Concentration of gas in water
D	Diffusivity coefficient
E	Latet heat flux
E_v	Evaporation
F	Net flux
g	Acceleration due to gravity
H	Sensible heat flux
k	Gas transfer velocity
k_a	Air-side resistance
k_n	Wave number
k_w	Water-side resistance
L	Obukhov Length
L_v	Latent heat of vaporization
Q	Net Radiation
q	Specific humidity
q_*	Scaling specific humidity
Q_s	Short Wave Radiation
Q_L	Long Wave Radiation
Q_H	Sensible Heat Flux

Q_{LV}	Latent Heat Flux
R	Ideal gas constant
R_B	Breaking wave parameter
R_b	Bulk Richardson number
R_e	Reynold's number
R_i	Richardson number
r_c	Mixing ratio
Sc	Schmidt number
T	Temperature
u	Velocity
u'	Perturbation from mean horizontal wind velocity
u_*	Frictional velocity
W	White capping coverage area
w'	Perturbation from mean vertical wind velocity
z	Height of measurement
z_0	Roughness length of momentum
z_{0h}	Roughness length of heat
z_{0q}	Roughness length of specific humidity
α	Solubility coefficient
χ_c	Mass concentration of CO_2
ε	Energy dissipation
κ	von Karman constant
ν	Kinematic viscosity
Ω	Angular velocity
ω_p	Spectral peak angular frequency of waves
ϕ	Roll
ψ	Yaw
ψ_h	Stability function for sensible heat
ψ_m	Stability function for momentum
ψ_q	Stability function for latent heat
ρ	Density of air
τ	Drag
Θ	Pitch

θ	Virtual temperature
θ'	Perturbation from mean virtual temperature
θ_*	Scaling temperature
ζ	Stability parameter

Chapter 1

Introduction

The Earth is an integrated system that consists of four main components or subsystems: the atmosphere, hydrosphere, lithosphere, and biosphere. These subsystems interact and are interconnected with each other. The atmosphere is the layer of gases that lies above the surface of the Earth and is held to its surface by gravity. The hydrosphere is the component of Earth, that consists of water in all its three phases. The lithosphere is the part of the Earth system that is composed of rocks and minerals, which consists of the Earth's outer solid outer crust, the inner core, and the inner molten mantel. The biosphere comprises of Earth's living things, which can be found in all other three subsystems of the Earth. Humans are a part of the biosphere, and human activities have an important impact on all the four components of the Earth. All the Earth processes are a result of the energy and mass flowing across and within the Earth's systems. The rate of movement across the subsystems is termed as flux. Energy is transferred across and between the systems in three ways: radiation, convection, and conduction.

1.1 Air-Sea Interactions

The atmosphere and hydrosphere interact through the exchange of heat, momentum, and mass. Oceans are a major component of the hydrosphere, and they cover over 71% of the Earth's surface. Oceans have a high heat holding capacity compared to that of the atmosphere and transport heat across latitudes through ocean circulation and to the atmosphere across the air-sea interface through sensible and latent heat (Pickard and

Emery, 1961). The air-sea fluxes are governed by processes acting on the interface as well as the boundary layer processes that influence the vertical transport. The transport processes that govern the exchange are the molecular diffusion and turbulence, both these aim at restoring equilibrium. In most cases, turbulent transport is more effective compared to that of molecular diffusion. The atmospheric processes which govern most of the air-sea exchanges are turbulent transport through the Atmospheric Boundary Layer (ABL). The Oceanic Boundary Layer (OBL) influences air-sea fluxes through mixing, bubble distributions, and wave breaking.

The understanding of weather and climate system of the Earth system is essential to humankind to predict and forecast the future, thus making it vital for us to understand the physics of these systems and how they influence each other. Understanding the physical processes that drive the exchange of momentum, heat, water vapor, and gases at the air-sea interface are vital as these are significant drivers of the weather and climate as momentum and heat fluxes at the interface influence the mixing layer and energy transport in the oceans. Over most of the oceans, latent heat flux (LHF) is comparatively higher than the sensible heat flux (SHF). It represents the water vapor supplied from the oceans to the atmosphere, determining the precipitation across the globe. However, understanding of the physical processes that drive the air-sea exchange is limited due to the lack of observed turbulent flux measurements over the ocean.

1.1.1 Boundary Layer

A boundary layer is defined as a layer near the interface where the effects of shear are significant. Both the ABL and OBL governs Air-sea fluxes. The layers of ABL include the interfacial or near-surface layer, surface or constant flux layer, mixed layer, and entrainment zone. A schematic of ABL evolution with a diurnal cycle is shown in Figure 1.1 (Stull, 2012). The ABL and OBL are similar, but the time and length scales differ due to the density of the media. The ABL has a depth ranging from tens of meters to several kilometers during stable and convective conditions, respectively. In the atmosphere, turbulent fluxes of momentum and mass tend to decrease monotonically with height throughout the depth of the boundary layer. Hence, a shallow layer above the surface, where the fluxes do not deviate significantly from the surface values, is defined as the constant flux layer. This layer usually extends to about 20-50 m. The

OBL is 5-50 m thick depending on stratification and wind speeds. Processes unique to the OBL are wave breaking and air entrainment. The sea surface sub-layer is involved with the transport of heat, momentum, and mass across the interface. The thickness of viscous, thermal, and diffusion molecular sub-layers at the interface is associated with the length scales of the turbulence; typically, molecular sub-layers extend from the surface to about 1500 μm (viscous sub-layer), 500 μm (thermal sub-layer), and 50 μm (diffusion sub-layer) (Csanady, 2001). The thickness of the molecular sub-layer depends on air-sea interaction, which in turn depends on wind stress, heat, salinity, and waves.

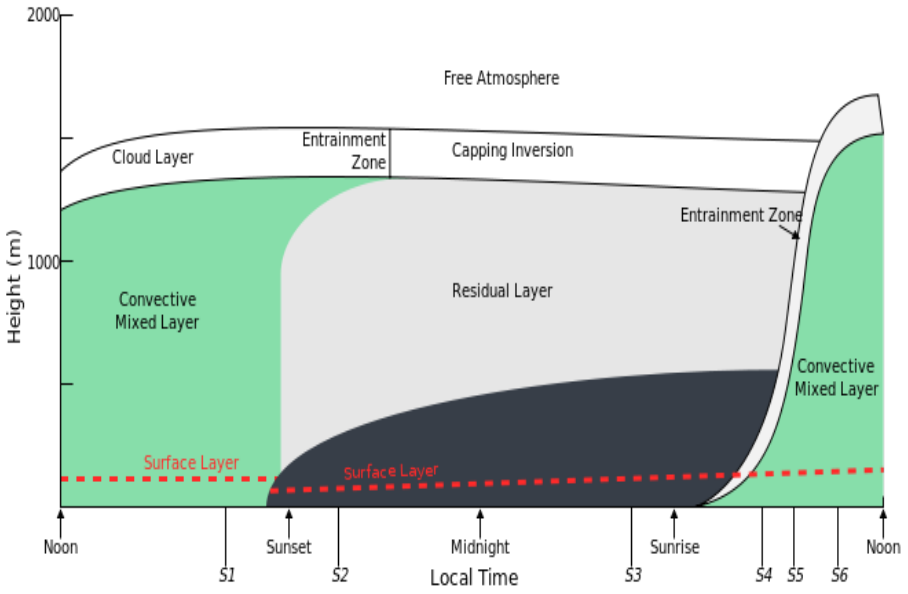

FIGURE 1.1: *Evolution of diurnal structure of Atmospheric Boundary Layer with local time. (From Stull (2012))*

Winds transfer energy into the water, impacting the surface by creating surface waves, which in turn affects the atmosphere's boundary layer. Mass is exchanged across the air-sea interface, having implications for water vapor in the atmosphere and trace gas concentrations in both the ocean and air (Csanady, 2001).

Mass transfer across the air-sea interface is important for the global budget of various gases like carbon dioxide (CO_2), oxygen (O_2), nitrous oxide, methane, dimethylsulfide (DMS), and volatile pollutants. Air-sea gas exchange influences air quality, weather, and water quality. Oceans can act as a sink for anthropogenic greenhouse gases. Gas exchange is also important in atmospheric radiative transfer - DMS acts as a precursor to cloud condensation nuclei (CCN), which in turn affects the radiative forcing through direct and indirect aerosol effects (Blomquist et al., 2006). In addition, the air-sea

exchange of gases is important for the chemical composition of the ocean (Carpenter et al., 2012).

1.1.1.1 Turbulence

Turbulence is characterized by chaotic motions that can be visualized as different sized eddies, which are responsible for the transfer of heat, momentum, and mass. The strengths of different scale eddies define the turbulence spectrum. The turbulence spectra is divided into three regions (as shown in Figure 1.2: low-frequency range, which is energy-containing region where turbulent energy is produced from the mean flow; an intermediate frequency range (inertial sub-range 0.01-5 Hz) where energy is transferred from large eddies to smaller eddies due to energy cascading, and there is no production of turbulence, and the flow is isotropic; high-frequency range where smaller eddies dissipate turbulent kinetic energy into heat by molecular viscosity. (Stull, 2012).

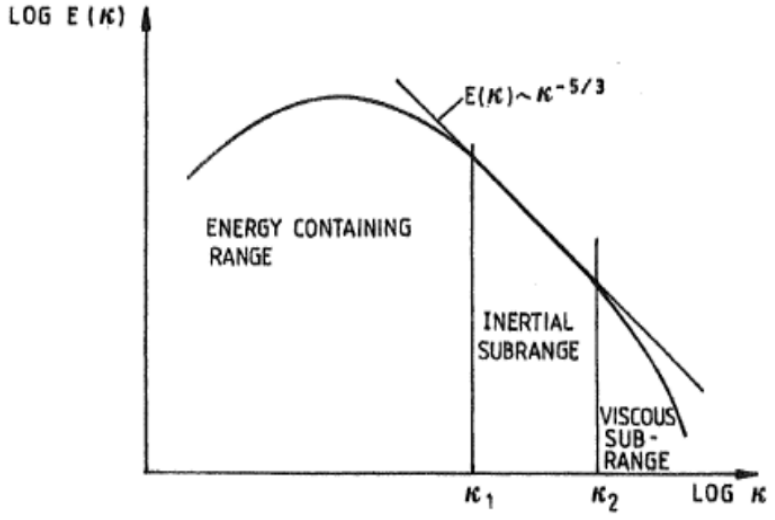

FIGURE 1.2: *Turbulence energy spectra, including different regimes. (From Högström et al. (1989))*

Energy dissipation is more efficient at the sharpest velocity gradients, therefore, at the smallest scales. Small eddies have a short length scale and short time scale, causing them to respond quickly to the change in the mean flow. According to Kolmogorov theory, the shape of the spectra depends only on the energy dissipation (ε) and the wave number

(k_n). Using the dimensional analysis, the energy spectra ($E(k_n)$) can be expressed as:

$$E(k) = a\varepsilon^{2/3}k_n^{-5/3} \tag{1.1}$$

Where a denotes the Kolmogorov constant equal to 0.52 (Högström, 1996).

1.2 Momentum Flux

The momentum flux or wind stress (τ) between the atmosphere and oceans is the transfer of horizontal momentum caused by the drag on the sea surface by the wind. The drag is of two types, the skin frictional or "skin" drag and the wave or "form" drag. The skin friction drag arises due to the molecular interaction at the interface, and the form drag arises due to the waves (Donelan et al., 2012).

The turbulent fluxes can be measured directly using various methods, traditionally the "profile method" uses logarithmic profile fitting to the wind speeds to estimate the roughness length z_0 or alternatively a drag coefficient C_D. More recently, the "inertial dissipation method" is being used, this assumes a balance of the generation and dissipation of the turbulent fluctuations. Similarity theory (discussed in section 1.2.2) and the dissipation energy from the observed spectrum in the inertial subrange is used to compute the fluxes. The most recent, state of the art, eddy covariance or eddy correlation technique, is the purest form to determine fluxes in the ABL. The flux is given as $\rho\overline{u'w'}$, where w' denotes perturbation from mean of the vertical wind velocity, u' denotes fluctuation from mean horizontal wind speed, and overline denotes a time average of sufficient length to capture turbulent frequencies which may vary depending on stationarity of the data and ρ denotes the density of the air. A detailed description, challenges faced, and corrections to be applied to the data to compute fluxes through the eddy covariance technique are described in Chapter 2.

Accurate calculations of regional and global air-sea fluxes play an important role in the performance of the weather and climate models. In climate and Numerical Weather Prediction (NWP) models, these air-sea fluxes are parameterized using bulk methods, which are modeled in terms of mean wind speed. These bulk models use Monin-Obukhov Similarity Theory (MOST) and Charnock's relation in predicting the momentum and heat fluxes, which is an iterative process. However, quantifying the air-sea fluxes requires

turbulent eddies to be explicitly resolved, which is not possible using the bulk methods. Currently, the available flux products are highly uncertain, as they are based on the inaccurate flux algorithms and uncertain observational quantities, which in turn limit the ability to assess numerical models based on flux data sets.

1.2.1 Charnock's Law

Charnock (1955) has characterized the distribution of wind speed with height over the surface of a reservoir in the form of:

$$\frac{u}{u_*} = \frac{1}{\kappa} log \frac{gz}{{u_*}^2} + C \tag{1.2}$$

where u is the wind speed at a height z above the surface, u_* is the friction velocity, g is the acceleration due to gravity, κ is the von-Karman constant and C is the constant, whose value is approximately equal to 12.5. Csanady (2001) has given an alternative form of Charnock's law as:

$$C_D = (C - 2\kappa^{-1} ln[u_*/\sqrt{gz}])^{-2} \tag{1.3}$$

where, C_D is the drag coefficient.

Over a roughed solid surface with a grain size of mean diameter r, the velocity distribution is given as:

$$\frac{U(z)}{u_*} = \frac{1}{\kappa} log \frac{z}{r} + 8.5 \tag{1.4}$$

where r is the mean sand grain diameter. A comparison with the Charnock's law with the rough surface gives

$$r = 3.064 \frac{u_*^2}{g} \tag{1.5}$$

The air-sea momentum transfer expressed as a function of roughness parameter z_0, is derived by substituting r and C:

$$\frac{U(z)}{u_*} = \frac{1}{\kappa} log \frac{z}{z_0} \tag{1.6}$$

The parameter z_0 according to Charnock's law, with constant of 12.5 is:

$$z_0 = 0.011\frac{u_*^2}{g} \tag{1.7}$$

The Charnock's Law studies the turbulent properties of the air in the constant stress layer, where the flow depends only on the velocity and length scales; however, it is not that simple as the air density varies due to heating, cooling or due to different percentage of humidity in the air. To account for these, buoyancy terms are to be included.

1.2.2 Monin-Obukhov Similarity Theory

Monin and Obukhov (Stull, 2012) using Buckingham Π theorem gave the dimensionless profiles of temperature and wind in the surface layer as a functions of non-dimensional parameter, ζ which is defined as z/L. Where L is the Obukhov length, $L = -\frac{u_*^3\theta}{g\kappa\overline{w'\theta'}}$, where u_*, the friction velocity is given as $(\overline{w'u'}^2 + \overline{w'v'}^2)^{1/4}$, g is acceleration due to gravity, θ is the virtual temperature, θ' is the perturbation from mean virtual temperature. In accordance to the dimensionless parameter, $\zeta = z/L$, the wind profile is written as:

$$\frac{\partial U}{\partial z}\left(\frac{\kappa z}{u_*}\right) = \phi(z/L) \tag{1.8}$$

where $\phi(z/L)$ is a function developed for different cases by different researchers over a period of time for different stability conditions. For neutral conditions, $\phi(z/L)$ must tend to unity. Integrating the velocity profile, we get:

$$u(z) = \frac{u_*}{\kappa}\left[ln\frac{z}{z_0} - \psi_m(\zeta)\right] \tag{1.9}$$

where ζ is the stability parameter and the function $\psi_m(\zeta)$ as follows by Businger et al. (1971)

$$\psi_m = 2ln\left(\frac{1+x}{2}\right) + ln\left(\frac{1+x^2}{2}\right) - 2\tan^{-1}(x) + \frac{\pi}{2} \tag{1.10}$$

where

$$x = (1 - 16\zeta)^{1/4} \tag{1.11}$$

for unstable conditions and

$$\psi_m = -5 * \zeta \tag{1.12}$$

for stable conditions.

1.3 Sensible and Latent Heat Fluxes

A complex thermodynamic interaction occurs at the air-sea interface. It receives short-wave radiation from the sun, reflects a fraction of it, allowing the rest to pass through the warm top surface of the ocean. The warm upper ocean interacts with the atmosphere by emitting the long-wave radiation back to the atmosphere and the radiative transfer across the interface. The rate of heat storage in oceans is given as

$$Q = Q_S - Q_L - Q_H - Q_{Lv} \tag{1.13}$$

Where Q is the net heat flux, Q_S is the short wave radiation absorbed, Q_L is the net upward long-wave radiation, Q_H is the surface sensible heat flux and Q_{Lv} is the latent heat (Pickard and Emery, 1961). The incoming short wave radiation depends on solar elevation, clouds, and aerosols and is absorbed in the top few meters, increasing the heat content of the oceans. The albedo of oceans is less than 10%, 90% of the incoming SW radiation is absorbed by the oceans. The short wave radiation heats up the ocean boundary layer and the ocean radiates the heat into the atmosphere like a black body by long-wave radiation, which is proportional to the fourth power of the sea surface temperature. The net long-wave radiation is the amount of energy lost or gained by the oceans, which is the difference of the long-wave radiation radiated by the surface ocean, and the long-wave radiation absorbed from the atmosphere. Sensible heat is the amount of infrared energy lost or gain at the surface by conduction from the air. Latent heat is the rate of heat loss or gain by evaporation or condensation. Latent heat of vapourization ($Q_{Lv} = E_v L_v$ where E_v is the rate of evaporation, and L_v is the latent heat of vaporization) is the heat taken to evaporate water.

In turbulent flow, Reynolds fluxes of temperature and humidity are the main drivers of heat and water vapor transport across the interface in the ABL which is similar to that of the momentum transfer, while the difference being that heat is due to molecular conduction or diffusion while for the momentum it is molecular (viscous) and pressure mechanism. The heat transfer is a complex interaction of physical processes like conduction, wind waves, eddies, and sea spray.

As in the case of momentum transfer, the temperature and specific humidity profiles are given as:

$$\theta(z) - \theta_s = \frac{\theta_*}{\kappa}\left[ln\frac{z}{z_{0h}} - \psi_h(\zeta)\right] \tag{1.14}$$

$$q(z) - q_s = \frac{q_*}{\kappa}\left[ln\frac{z}{z_{0q}} - \psi_q(\zeta)\right] \tag{1.15}$$

where $\phi_h(\zeta)$ and $\phi_q(\zeta)$ are stability functions z_{0h} z_{0q} are roughness lengths of heat and moisture, $\zeta = z/L$ is the stability parameter which is defined in 1.2.2, $\theta_* = -\overline{w'\theta'}/u_*$ is the scaling temperature and $q_* = -\overline{w'q'}/u_*$ is the scaling specific humidity.

$$\psi_h = \psi_q = 2ln\left(\frac{1+x^2}{2}\right) \tag{1.16}$$

where

$$x = (1 - 16\zeta)^{1/4} \tag{1.17}$$

for unstable conditions and

$$\psi_h = \psi_q = -5 * \zeta \tag{1.18}$$

for stable conditions. The stability functions 1.10, 1.12, 1.16 and 1.18 are not the only published literature, a few of the stability functions are given in A.1.

The role of atmospheric surface layer stability in regulating turbulent fluxes of latent heat and sensible heat over oceans is one that is less well understood, given the complex interaction between stability and other atmospheric variables.

Most studies use the bulk methods to estimate the fluxes to study the effect of stability on fluxes, however quantifying air-sea fluxes requires turbulent eddies to be explicitly resolved, which is not possible using bulk algorithms. Bulk methods use MOST and Charnock's relations to parameterize the fluxes in models. However, the physical interpretation of MOST can be ambiguous due to self-correlation and circular dependence (Vickers et al., 2015) as MOST employs an iterative process to predict turbulent fluxes in terms of exchange coefficients that depend on stability functions and thus on turbulent fluxes through Obukhov length. Kara et al. (2005) derived the exchange coefficients in terms of polynomial functions of wind speed and temperature and relative humidity. This study used COARE (Coupled Ocean-Atmosphere Response Experiment) model exchange coefficients to formulate the equations. Vickers et al. (2015) used aircraft based

eddy correlation measurements to develop a formulation for friction velocity that depends on wind speed and stability parameter, bulk Richardson number which does not require MOST, while Zou et al. (2017) gave exchange coefficients as a linear function of stability parameter Richardson number using the turbulent measurements from a platform. However, there is no study to represent fluxes in terms of stability without using turbulent quantities.

1.4 CO_2 Flux

Gas transfer across the interface is due to the concentration difference in air and water. The net flux is transferred from the phase of higher concentration to the phase of lower concentration. The main processes through which transfer occurs is mass diffusion and turbulence (Liss and Merlivat, 1986). As turbulence increases, the size of turbulent eddies decreases, increasing the small-scale fluctuations (the dissipation scale decreases) which thins the diffusion sublayer and increases gas transfer that is limited by the diffusive boundary layer. Figure 1.3 shows the atmospheric and oceanic mass boundary layers at the interface.

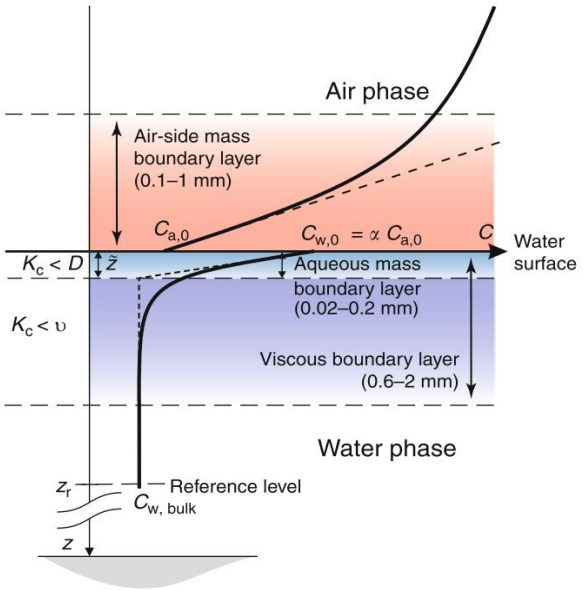

FIGURE 1.3: *Concentration profile of a tracer gas with solubility α =3 in boundary layers at the interface (From Liss et al. (2014))*

Gas transfer velocity is modeled in terms of Schmidt number ($Sc = \nu/D$, where ν is kinematic viscosity ($m^2 s^{-1}$) and D is diffusion coefficient ($m^2 s^{-1}$)). The flux of slightly

soluble non-reactive gases across the air-sea interface, $F(kgs^{-1}m^{-2})$ is defined as the product of gas transfer velocity, $k(m/s)$ and the concentration difference,

$$F = k(C_w - C_o) \tag{1.19}$$

Where C_w is the concentration of gas in a well-mixed boundary layer of water, and C_o is the concentration of gas at the interface. As per Henry's law, in equilibrium conditions, the concentration at the interface is equal to the product of the solubility and concentration in air.

$$F = k(C_w - \alpha C_a) \tag{1.20}$$

Where C_a is the concentration of gas in the air, and α is the solubility coefficient. The concentration profile in the aqueous boundary layer depends on solubility. As the temperature increases, solubility decreases. For a specific gas, solubility in saline water is about 20% less than that of in freshwater (Matson and Harriss, 2009).

As the temperature of water increases, the diffusivity coefficient increases, decreasing the Schmidt number. The relation between diffusivity coefficient and the temperature is given as $D = Ae^{-E_a/RT}$ where A is a gas specific constant of proportionality, E_a is a gas specific activation energy of diffusion, R is the ideal gas constant and T is temperature. Figure 1.4 shows solubility, Schmidt number dependence for various gases. Transfer resistance is inverse of the transfer velocity. The total transfer resistance is the sum of airside ($\frac{1}{k_a}$) and waterside resistances ($\frac{1}{k_w}$)

$$\frac{1}{k_t} = \frac{1}{k_w} + \alpha\frac{1}{k_a} \tag{1.21}$$

depending on the solubility of the tracer, either air-side or water-side is dominant. For slightly soluble gases, the gas transfer is water side controlled and for highly soluble gases, the transfer is air side controlled.

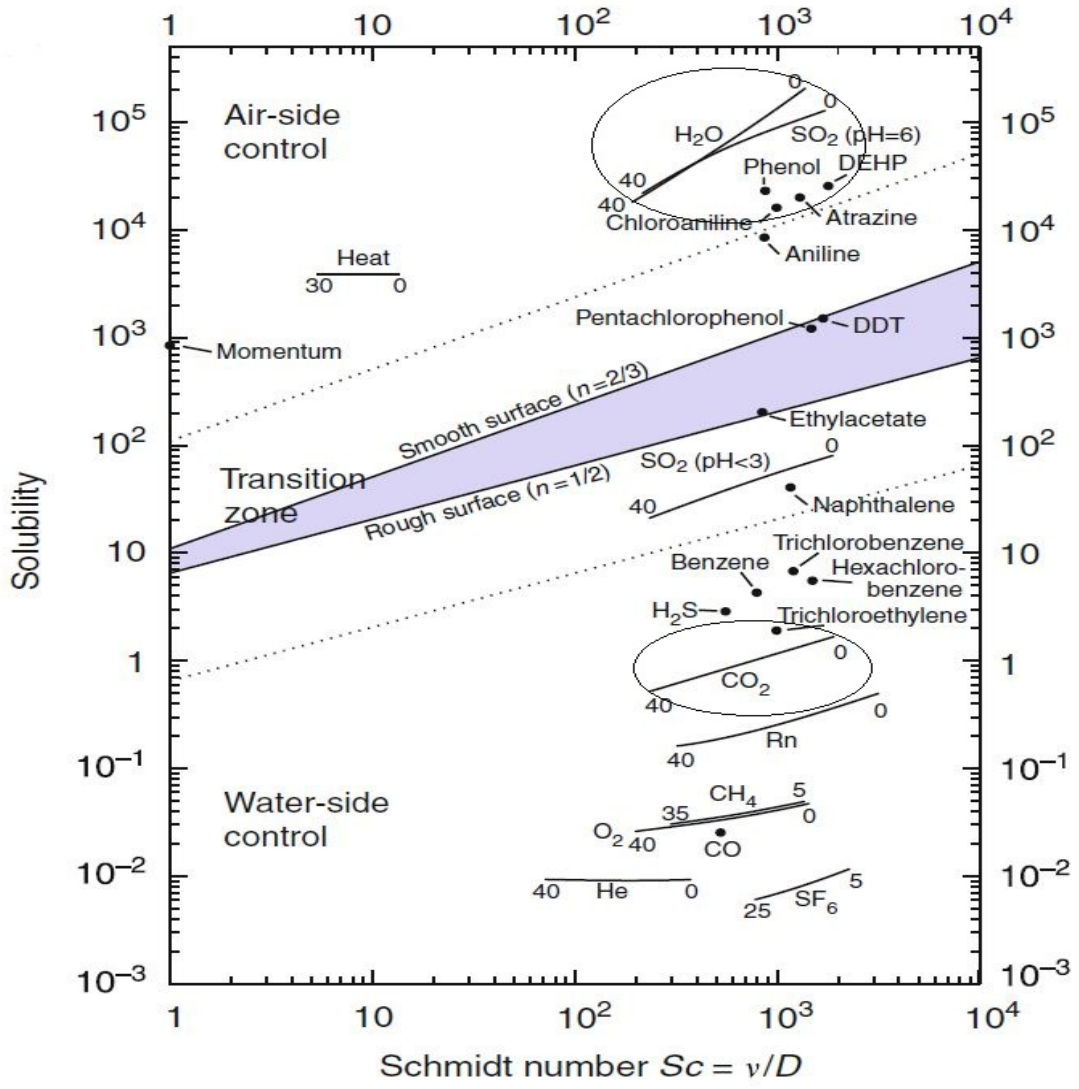

FIGURE 1.4: *Schmidt number/solubility diagram including various volatile tracers, momentum, and heat for a temperature range as indicated. Filled circles refer to a temperature of 25° C. The regions for air-side, mixed, and waterside control to the transfer process between gas and liquid phase are marked. At the solid lines, the transfer resistance is equal in both phases (From Jähne and Haußecker (1998))*

1.4.1 Processes influencing gas transfer

Figure 1.5 shows the major processes affecting the air-sea transfer of gases, which are wave breaking, small and large scale turbulence, waves, bubbles, spray, surfactants, rain, chemical, and biological properties. The wind generates turbulence at the air-water interface through shear or through waves. Eddies close to the surface bring bulk water to the surface, enhancing the gas transfer across the surface. Waves affect roughness (the height for which the extrapolation of the log profile yields zero wind speed) and

group speeds (velocity at which wave amplitudes travel), which are affected by wind speeds, wind duration, fetch, the shape of the ocean basin, water depth, and atmospheric boundary layer. Frew et al. (2004) has shown that the gas transfer velocity correlates well with the mean square slope of waves and wind speeds.

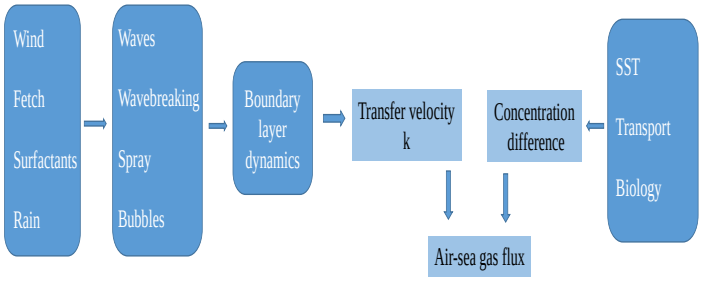

FIGURE 1.5: *Schematic of factors affecting air-sea gas transfer of CO_2 (adapted from Wanninkhof et al. (2009))*

Microbreaking is breaking of short wind waves (wavelengths of centimeters to meter and amplitude of 0.01-0.1 m) without any visible air entrainment; they disturb the molecular boundary layer, which is important in the air-sea gas exchange. Microbreaking directly enhances heat and gas transfer, producing surface roughness that contributes to the mean square slope of the waves. Wave breaking plays a vital role in transporting the surface water to the turbulent domain below. Zappa et al. (2004) has used active controlled flux technique for heat transfer and mass balance for gas transfer and found a correlation between microbreaking coverage area and heat and gas transfer, and also found that there is a correlation between mean square wave slope and coverage area of microbreaking. Wave breaking occurs at moderate to high wind speeds, generating air bubbles and spray. Air bubbles collapse, converting surface free energy to kinetic energy that ejects a vertical jet from the center of the bubble cavity by breaking into drops. Sea spray releases water vapor into the atmosphere and also exchanges sensible

heat with the above lying atmosphere, thereby absorbing sensible heat to evaporate. The re-entrant spray reduces the surface temperature. Gas transfer is correlated with white-capping coverage area (W) in wave breaking with air entrainment process (Asher et al., 1996). It is seen that gases with lower solubilities have a more significant bubble enhancement compared to that of gases with higher solubilities. Zhao and Toba (2001) has given white-capping coverage area as a function of wave age (β), wave period (T_s), wind speed (U), friction velocity (u_*), and breaking wave parameter (R_B).

$$\begin{aligned} W &= 4.69 \times 10^{-3} \beta^{1.27} \\ W &= 3.14 \times 10^{-2} T_s^{1.82} \\ W &= 2.98 \times 10^{-5} U^{4.04} \\ W &= 8.59 \times u_*^{3.42} \\ W &= 3.88 \times 10^{-5} R_B^{1.09} \end{aligned} \tag{1.22}$$

Zhao et al. (2003) gave a relationship between gas transfer velocity and breaking wave parameter as

$$k = 0.13 R_B^{0.63} \tag{1.23}$$

where R_B is the breaking wave parameter given as $R_B = u_*^2/\omega_p \nu$, ω_p is the spectral peak angular frequency of waves, u_* is the friction velocity, and ν is the kinematic viscosity of air.

Gas transfer across the interface does not occur only through molecular diffusion but also through bubbles and sea spray. Bubbles are primarily generated by the air entrainment within breaking waves. Bubbles and wave-breaking enhances surface turbulence and may enhance gas transfer rates (Crosswell, 2015). The vertical entrainment of bubbles is found to be greatly influenced by the wave structures (Hwang et al., 1990). Bubble populations on the surface are influenced by surface wave height and wind stress. It is suggested that bubble mediated transfer is highly effective for less soluble gases like CO_2 compared to that of more soluble gases like DMS. The dependence of bubble mediated transfer of gases for more soluble gases is yet to be known. (Woolf, 1993) has proposed that the total gas transfer is a combination of diffusional flux and bubble mediated flux.

The net flux (F) is given as:

$$F = (K_0 + K_b)[C - \alpha p(1 + \delta)] \tag{1.24}$$

where K_0 is the transfer for direct exchange, K_b is the bubble contribution to the gas transfer, α is solubility, p is the partial pressure of the gas in the atmosphere, C is the concentration of gas in water, and δ denotes the equilibrium supersaturation.

Surfactants inhibit gas exchange by either forming an insoluble surfactant film, by forming a condensed monolayer on the surface or by providing an additional liquid surface that provides resistance to mass transfer (Asher and Wanninkhof (1998)). Surfactants are important in low wind speeds as films easily disperse with the winds. Surfactants reduce the roughness, thereby reducing the turbulence and wave breaking. However, there is no clear understanding of the effect of surfactants at high winds as the surfactants are brought back to the surface by bubbles. In the intermediate wind speed regime, as the wind speeds increase, the effect of surfactants on gas transfer decreases (Salter et al., 2011). The influence of surfactants on gas fluxes on a global scale is unknown.

Turk et al. (2010) has shown that due to the effect of rain, the Western Equatorial Pacific has turned to a sink from a source of carbon dioxide. Rain causes surface chemical dilution reducing surface salinity, total alkalinity, and dissolved inorganic carbon, thereby decreasing the partial pressure of carbon dioxide at the surface. Rain enhances the turbulence and bubbles at the surface, thereby increasing gas transfer across the interface. Takagaki and Komori (2007) have shown that mass transfer across the surface is correlated with mean vertical momentum flux of rain, which is a function of rain rate and velocity of the raindrop. Komori et al. (2007) has studied the effect of rain on CO_2 transfer across the air-sea interface and has shown that the total effect of rainfall globally on transfer is less than 5%.

1.4.2 Gas transfer parameterization with wind speeds

Gas transfer parameterization is necessary to represent the exchange of gases across the air-water interface in any model. Figure 1.6 shows global surface wind speeds for January 2014 from ERA-Interim data (Dee et al., 2011). We can observe that the wind speeds are higher over the oceans, especially over the Southern Ocean, North Pacific,

and North Atlantic. There is a limited understanding of gas transfer at high wind speeds as it is a complex case with a combination of breaking waves, bubbles, spray, and direct transfer across the interface. Garbe et al. (2014) has compared the gas transfer velocities obtained from field experiments using mass balance and eddy covariance methods and has found that the magnitude of the gas transfer velocities is higher when using eddy covariance.

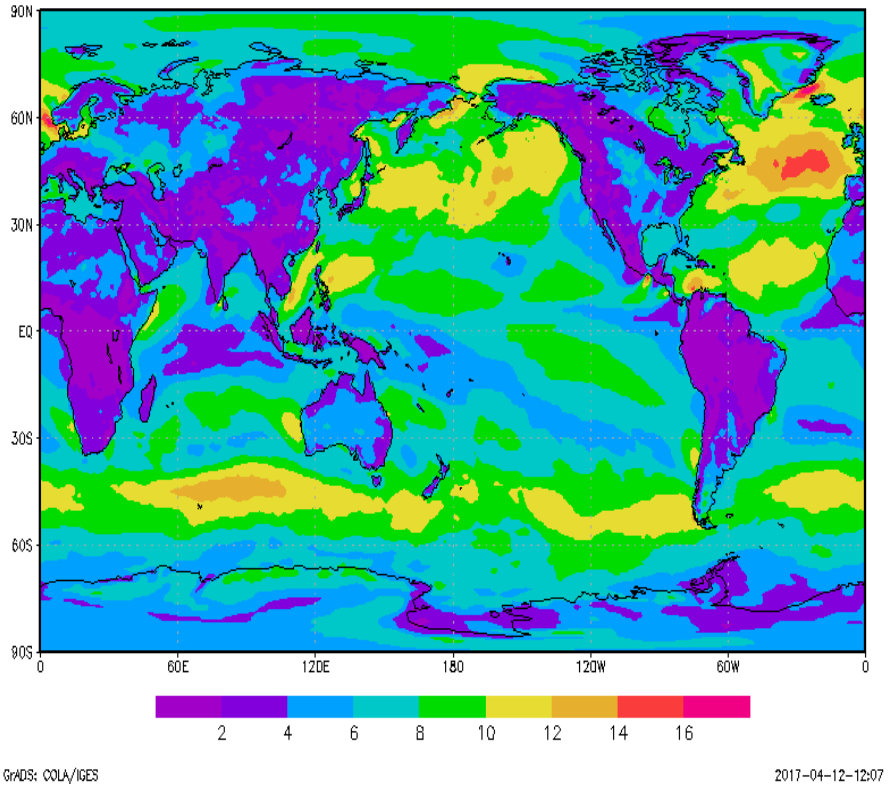

FIGURE 1.6: *Global wind speeds for January 2014 from ERA-Interim data*

Table 1.1 gives the literature of parameterizations for gas transfer velocity. These gas parameterizations proposed are based on field and laboratory experiments, ranging from a linear relationship to quadratic, cubic, or power-law with wind speeds.

Study	**Parameterization**
Liss and Merlivat (1986)	$k = 0.17u_{10}$ for $u_{10} \leq 3.6ms^{-1}$ $k = 2.85u_{10} - 9.65$ for $3.6ms^{-1} \leq u_{10} \leq 13ms^{-1}$ $k = 5.9u_{10} - 49.3$ for $u_{10} \geq 13ms^{-1}$
Wanninkhof (1992)	$k = 0.31u_{10}^2(Sc/660)^{-1/2}$ for instantaneous wind speeds $k = 0.39u_{10}^2(Sc/660)^{-1/2}$ for integrated wind speeds
Wanninkhof and McGillis (1999)	$k = 0.0283u_{10}^3(Sc/660)^{-1/2}$ for short integration time $k = (1.09u_{10} - 0.333u_{10}^2 + 0.078u_{10}^3)(Sc/660)^{-1/2}$ for long integration time
Nightingale et al. (2000b)	$k = 0.222u_{10}^2 + 0.333u_{10}$
Nightingale et al. (2000a)	$k_{600} = 0.24u_{10}^2 + 0.061u_{10}$
Ho et al. (2006)	$k_{600} = (0.266 \pm 0.019)u_{10}^2$
McGillis et al. (2001)	$k_{660} = 3.3 + 0.026u_{10}^3$
McGillis et al. (2004)	$k_{660} = 8.2 + 0.014u_{10}^3$
McNeil and D'Asaro (2007)	$k = 14 + 0.0002925u_{10}^{3.742}$
Iwano et al. (2013)	$k = 1.02u_{10}^{1.25}$ for $u_{10} \leq 33.6m/s$ and $k = 5.32 \times 10^{-4}u_{10}^{3.4}$ for $u_{10} \geq 33.6m/s$
Zemmelink et al. (2004)	$k = 0.6u_{10}^2$
Rutgersson et al. (2016)	$k = 0.074u_{10}^3$
Miller et al. (2009)	$k = 3u_{10} - 2.5$
Butterworth and Miller (2016)	$k = 0.245u_{10n}^2 + 1.3$

TABLE 1.1: List of gas transfer parameterizations with wind speeds taken from different literature.

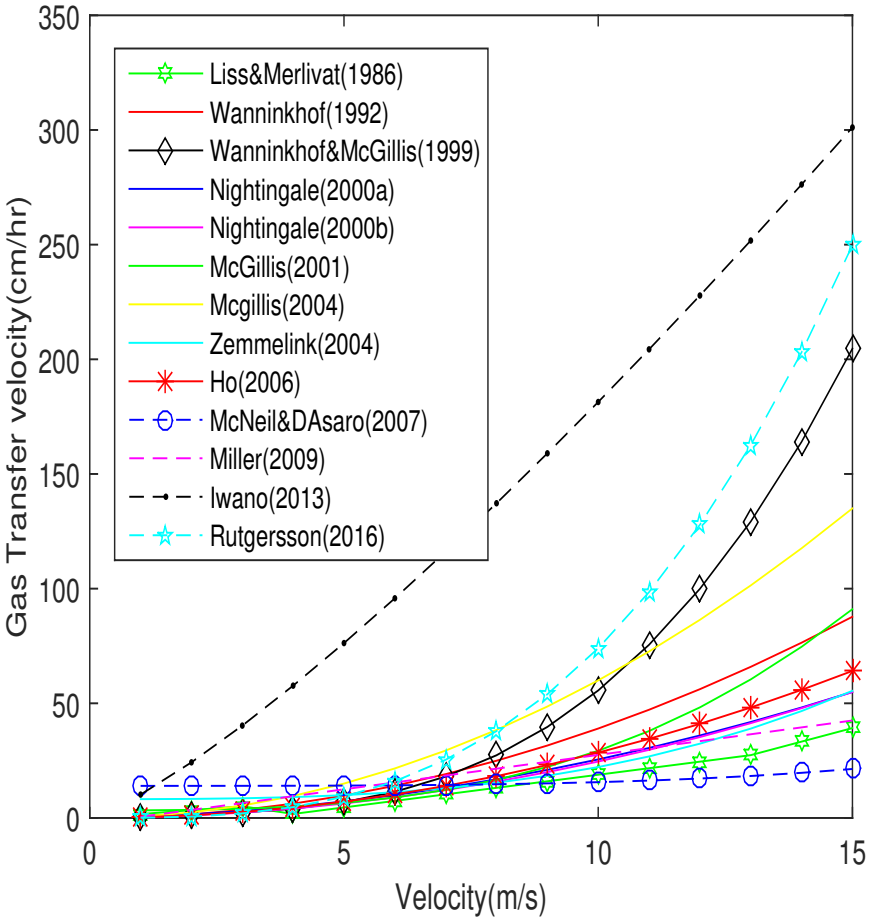

FIGURE 1.7: *Comparison of different wind speed relationships with transfer velocity equations from Table 1.1*

Figure 1.7 shows the variation of gas transfer velocity with the wind speed given by various researchers. It is seen that there is high variance in the gas transfer velocities at high wind speeds obtained by different parameterizations; hence, it is necessary to get an optimal gas transfer parameterization at high wind speeds. However, there are very few studies that studied gas transfer at high wind speeds. It is extremely difficult to measure gas transfer in the real field; hence, laboratory experiments were conducted where the environment can be controlled. Krall and Jähne (2014) had performed wind-wave tank experiments at hurricane-strength wind speeds of about 67 m/s for hexa fluorobenzene and 1,4-difluorobenzene using a mass balance method and found higher transfer rates for hexa fluorobenzene compared to 1,4-difluorobenzene which is a lower soluble gas.

1.5 Objectives and outline of thesis

Objectives of this study are: Accurate parameterization of air-sea interactions is essential to quantify the fluxes across the interface to accurately predict the weather and climate. The current state of art climate and weather prediction models use bulk models to compute the fluxes; however, these bulk models, due to the self-correlation and circular dependence, are not accurate enough. In this study, we have used the ship's attitude and navigation data to verify if we can use the ship's data to correct the wind velocities for the platform motions instead of using an external collocated accelerometer to compute the fluxes through eddy covariance technique. This study aims to parameterize the fluxes using a simple model that is modeled in terms of bulk meteorological quantities.

The outline of this thesis is as follows: Chapter 1 provides a brief overview of the air-sea interface, and the processes that affect the fluxes, how these interfacial fluxes are parameterized. Chapter 2 addresses the Eddy covariance or eddy correlation technique. This chapter uses the accelerometer data to verify that the navigation data can be used to correct for ship's platform motions, to obtain the correct wind speeds to compute the fluxes. Chapter 3 addresses the calculation of neutral coefficients of fluxes and stability dependence of the fluxes. In this chapter, we parameterize the fluxes as a function of the wind speeds and bulk Richardson number. Chapter 4 deals with the calculations of carbon dioxide fluxes and the corrections that are applied to compute the fluxes. It also deals with the calculation of gas transfer velocity and its dependence on wind speeds and stability. The thesis concludes with a summary of key contributions from the present study along with the suggestions for possible extensions to the current work.

Chapter 2

Eddy Covariance

This chapter discusses the Eddy Covariance method in depth. The corrections and data processing required to calculate the fluxes using this method are discussed. Finally, if we can use the ship's navigation data to correct the platform motion corrections is characterized and discussed.

The Eddy Covariance or Eddy Correlation method is used to measure flux. It is a good estimate if the flux is constant with height. It is used in field experiments for flux measurements in constant flux layer, which is about 20-50 m in an unstable boundary layer (Aubinet et al., 2012). The momentum conservation equation is given by:

$$\frac{\partial \rho u_i}{\partial t} + \vec{\nabla}(\vec{u}\rho u_i) = S_i \tag{2.1}$$

where S_i represents the source or sink term, ρ is the density of air, ∇ represents the divergence $(\partial/\partial x, \partial/\partial y, \partial/\partial z)$, $\vec{u}$ represents the velocity vector. Applying Reynold's decomposition to the above equation leads to

$$\frac{\overline{\partial u}}{\partial t} + \overline{u}\frac{\partial \overline{u}}{\partial x} + \overline{v}\frac{\partial \overline{u}}{\partial y} + \overline{w}\frac{\partial \overline{u}}{\partial z} + \frac{\partial \overline{u'^2}}{\partial x} + \frac{\partial \overline{u'v'}}{\partial y} + \frac{\partial \overline{u'w'}}{\partial z} = 0 \tag{2.2}$$

assuming horizontal homogeneity and steady-state conditions, we obtain

$$\frac{\partial \overline{u'w'}}{\partial z} = 0 \tag{2.3}$$

where $\overline{u'w'}$ is the eddy covariance term, w' denotes variation from mean of the vertical wind velocity, u' denotes variation from mean horizontal wind speed and overline

denotes a time average of sufficient length to capture turbulent frequencies which may vary depending on the stationarity of the data. To capture the turbulent frequencies, high-frequency measurements are required (5 Hz to 40 Hz). The typical temporal and longitudinal length scales of the eddy covariance method is about an hour and about 100-2000 m. The equation suggests that the flux is constant with height.

For a scalar quantity, the horizontal velocity is replaced by the mixing ratio. To measure gas fluxes, high-frequency measurements of gas concentrations along with wind speeds are necessary, and due to this limitation, using the eddy covariance technique to estimate gas fluxes is restricted to CO_2, O_2, and DMS. However, this technique has been successfully tested for methanol, methane, nitrogen, nitrous oxide, ammonia, acetone (Yang et al., 2014; Carpenter et al., 2012; Blomquist et al., 2006; McGillis et al., 2001; Jähne and Haußecker, 1998).

Advantages: Eddy Covariance technique does not rely on assumptions about gas properties or approximations concerning the turbulent structure of the atmospheric boundary layer.

Disadvantages: Eddy Covariance technique requires rapid, high-precision measurement of atmospheric gas concentrations. The measured fluxes of gases for the co-varying flux of water vapor and temperature (the Webb effect (Webb et al., 1980)), salt contamination, and sensor separation are to be corrected for.

2.1 Eddy-Covariance - Moving Platform

The Eddy-Covariance method is mostly implemented on stable platforms over land surfaces. In the past two decades, Eddy Covariance has been successfully implemented on moving platforms over oceans. The challenge is that the turbulent components of velocity are contaminated by platform motion and flow distortion around the platform. The observed velocities require correction to obtain actual velocities and need transformation to the Earth's coordinate system before calculating fluxes.

2.2 Observations

The measurements used in this study were collected from the research vessel *R/V Investigator* during CAPRICORN-1 (Clouds, Aerosols, Precipitation, Radiation, and atmospherIc Composition over the southeRn oceaN) voyage. The field experiment was conducted between 14 March 2016 and 15 April 2016 to collect *in situ* observations of clouds, aerosol, precipitation, ocean properties and fluxes over the Australian sector of the Southern Ocean (Mace and Protat, 2018). The *R/V Investigator* started from Hobart, 43^{o}S, reached 53^{o}S before returning back to Hobart.

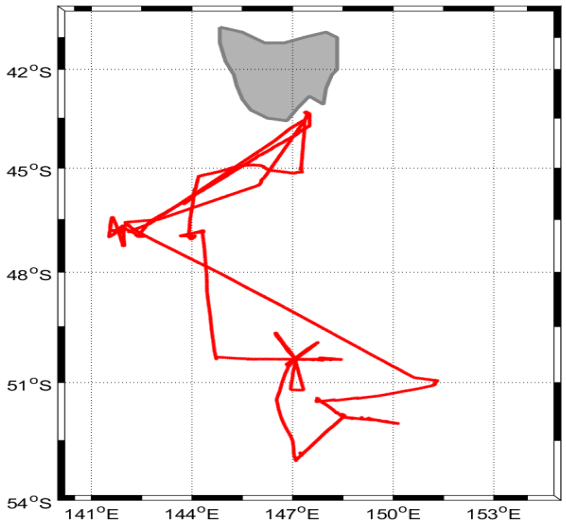

FIGURE 2.1: *R/V Investigator track during the CAPRICORN voyage during 14 March to 15 April to Australian sector of the Southern Ocean.*

The National Oceanic and Atmospheric Administration, Physical Sciences Division (NOAA PSD), has installed it's air-sea flux system on the front bow jackstaff of the ship, which is similar to that of the *R/V Brown*. The NOAA air-sea flux system consists of:

- A Metek uSonic-3 3-D ultrasonic anemometer, which measures u, v, w components of wind and sonic temperature at 10 Hz frequency.
- A Systron Donner motionpak unit, which measures the angular rates and linear accelerations at 10 Hz frequency.

- A Global Positioning System sensor, which receives Latitude, Longitude data at 1 Hz frequency
- A heading sensor, which measures the heading and roll of the ship at 10 Hz frequency.
- An Eppley Precision Spectral Pyranometer, which measures the solar downwelling radiative flux at 1 Hz averaged, and mean values stored at 1 min.
- Eppley Precision Infrared Radiometer, which measures Infra red downwelling radiative flux at 1 Hz frequency averaged, and mean values stored at 1 min.
- Vaisala HMT335 sensor, which measures temperature and humidity at 10 Hz frequency averaged, and mean values stored at 1 min.
- Vaisala PTB220 sensor, which measures pressure at 1 Hz frequency averaged, and mean values stored at 1 min.
- Floating YSI 46040 thermistor which measures the near-skin sea surface temperature at 1 Hz frequency averaged, and mean values stored at 1 min.
- ORG-815 DA optical precipitation sensor, which measures rain rate at 1 Hz frequency averaged, and mean values stored at 1 min.
- LICOR 7500 Open path Gas Analyzer, which measures the concentration of carbon dioxide and water vapor in air at 10 Hz frequency.

The flux system was installed on the foremast of the *R/V Investigator*. The anemometer and LICOR measurements were made at 21 m above the sea level, and the accelerometer was collocated with the anemometer and was placed at a distance of 0.7 m below the anemometer. The temperature and humidity measurements were made at 19.5 m above the sea surface, while the sea surface temperatures were measured at about 0.05 below the surface. The pyranometer and radiometer measurements were made at 12 m above the surface.

In this chapter, we have used the accelerometer data to correct the wind speeds which are contaminated by the platform motions of the ship. However, in the absence of a reliable accelerometer, it is hard to calculate the platform motions. Hence, we checked

if the ship's attitude and navigation data can be used to compute the platform motions, and used them to correct the anemometer measured wind speeds. Hence in the presence of a reliable accelerometer from the NOAA flux system, we concluded that the ship's attitude and navigation data could be used in the absence of an accelerometer.
The ship's attitude data is measured by the Seapath 330 Motion Reference Unit (MRU) (measures roll, heave, heading, pitch, vertical velocity, rotational rates) at 10 Hz frequency. The navigation data from the ship has latitude, longitude, speed, depth, roll, altitude, heave, pitch, heading measured at 1Hz frequency. The MRU was present at a distance of 36.437 m behind, 1.385 m towards starboard side, and 22.209 m below the anemometer.

2.3 Motion Corrections of Raw Data

Wind speeds measured on research vessels are contaminated by the linear velocities and angular velocities of the platform. Therefore the measured wind speeds are to be corrected for:

- Instantaneous tilt of the anemometer due to pitch, roll, and heading variations of the platform.
- Angular velocities at the anemometer due to rotation of the platform about the center of gravity.
- Translational velocities of the platform.

The corrected wind speeds are used to calculate the fluxes using eddy covariance. Here, to correct the wind speeds for motion corrections, I have used the basic approach given by Edson et al. (1998), where the rotational motion of the ship body is about its centre of gravity, and later corrected for by when the rotations measured are not about the centre of gravity. The equations are given by:

$$V_{true} = TV_{obs} + \Omega \times TP + V_{cg} \tag{2.4}$$

where V_{true} is the true wind speed in the Earth coordinate system, V_{obs} is the wind velocity in the platform reference, Ω is the angular velocity of the platform, P is the position vector of the wind sensor from the ship's center of gravity, T is the transformation matrix to transform from the platform frame of reference to the Earth frame and V_{cg} is the linear velocity at the center of gravity (cg) of the ship with respect to the Earth.

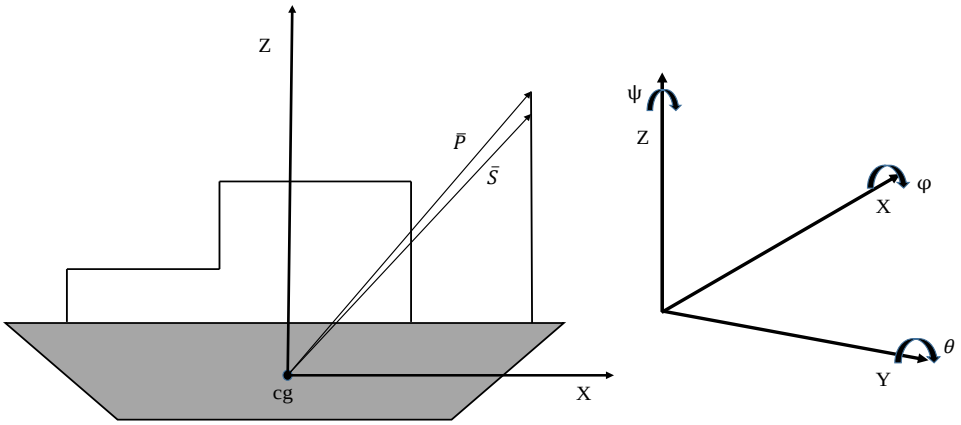

FIGURE 2.2: *Schematic of the ship showing the position of sensors and axes.*

When the motion measurement system is not at the center of gravity, the correction equation is given as

$$V_{true} = TV_{obs} + \Omega \times T(P - S) + V_{cg} \tag{2.5}$$

where $P - S$ is the position vector of wind vector with respect to the motion sensor. The transformation matrix is given as:
$T(\phi, \Theta, \psi) = A(\psi)A(\Theta)(\phi)$

$$= \begin{bmatrix} \cos(\psi) & \sin(\psi) & 0 \\ -\sin(\psi) & \cos(\psi) & 0 \\ 0 & 0 & 1 \end{bmatrix} \begin{bmatrix} \cos(\Theta) & 0 & \sin(\Theta) \\ 0 & 1 & 0 \\ -\sin(\Theta) & 0 & \cos(\Theta) \end{bmatrix} \begin{bmatrix} 1 & 0 & 0 \\ 0 & \cos(\phi) & -\sin(\phi) \\ 0 & \sin(\phi) & \cos(\phi) \end{bmatrix}$$

$$= \begin{bmatrix} \cos(\psi)\cos(\Theta) & \sin(\psi)\cos(\phi) + \cos(\psi)\sin(\Theta)\sin(\phi) & -\sin(\phi)\sin(\Theta) + \cos(\psi)\sin(\Theta)\cos(\phi) \\ -\sin(\phi)\cos(\Theta) & \cos(\psi)\cos(\phi) - \sin(\psi)\sin(\Theta)\sin(\phi) & -\sin(\Theta)\cos(\phi)\sin(\psi) - \sin(\phi)\cos(\psi) \\ -\sin(\Theta) & \cos(\Theta)\sin(\phi) & \cos(\Theta)\cos(\phi) \end{bmatrix}$$

where yaw angle ψ is positive for the ship's bow yawed clockwise from north, roll angle ϕ positive for the port side rolled up, and pitch angle Θ positive for the bow pitched down. Figure 2.2 shows the position of the sensors relative to the centre of gravity and the roll, pitch, and yaw angles.

The motionpak measures the linear accelerations and rotation rates. Hence we need to calculate the Euler angles to determine the transformation matrix. The Euler angles are calculated by integrating the angular rates and adding them on low frequency angles calculated from the horizontal acceleration components of the acceleration due to gravity, g, where, $\phi \approx \tan^{-1}(\ddot{y_p}/g)$ and $\Theta \approx \tan^{-1}(\ddot{x_p}/g)$. The two estimates are combined using complimentary filtering, where high-pass filtered rate sensor angle estimates are combined with low-pass filtered estimates from the accelerometers. A fourth-order Butterworth filter is used for complimentary filtering with a cutoff period of 30 s. The low-frequency yaw is obtained from the heading. The platform linear velocity and displacement are calculated by integrating and double integrating the linear accelerations in the Earth frame of reference. After each integration, signals are high-pass filtered to remove the low-frequency effects. The ship attitude and navigation data have roll and pitch angles measured, therefore requiring only yaw to be calculated. The yaw angles are calculated in a similar way that is calculated for accelerometer data.

The data obtained from the NOAA motionpak and ship's MRU are compared, and it was found that the NOAA data is leading the MRU data by 1.4 seconds, although the navigation data from NOAA package and the ship's NTP server were matching. This requires the lag corrections to be performed before correcting for the true winds. The lag found may vary with the position vector of the anemometer and the ship's motion reference unit. Hence the found lag is only for the anemometer mounted on the front mast of the ship..

The true wind speeds are calculated using Equation 2.4. The Figure 2.3 shows the raw, motion-corrected vertical wind speed and the platform velocity calculated from the

NOAA accelerometer data, while Figure 2.4 shows the raw, motion-corrected vertical winds from NOAA and ship's MRU data. The wind components relative to the Earth are used to compute the wind direction. The velocities are double rotated into the streamwise wind and single rotated counterclockwise back to Earth coordinates; then, these winds are to be added to the linear north and west components of velocity of the ship's centre of gravity which is calculated from the GPS data to remove the platform velocity. Finally, the azimuth angle is calculated, and the winds are rotated clockwise into streamwise winds (i.e., mean V and W are zero after the rotation).

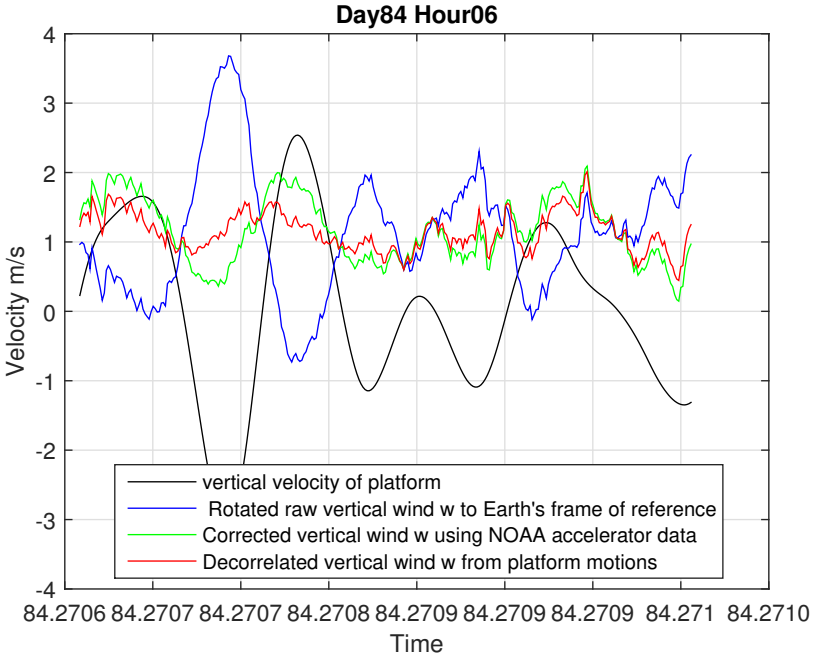

FIGURE 2.3: *Time series of the measured vertical velocity from sonic anemometer (raw), motion corrected vertical velocity from NOAA accelerometer, decorrelated vertical wind component and platform vertical velocity computed.*

Measured and motion-corrected latitudinal, lateral and vertical velocity spectra are shown in the figures 2.5(a)-2.5(c), where the green line is the power spectra for the measured raw winds, blue line is the power spectra for the winds that are corrected using the ship's MRU data and blue line is the power spectra for the winds that are corrected using the NOAA accelerometer data. In the Figure 2.5(a), vertical velocity spectra is shown, where a peak is visible due to the ship's motion in the raw data spectra at 0.25 Hz, and in the spectra of the corrected winds, the spectral peak is effectively removed. The spectra of the velocity for both the accelerometer and ship's corrected data is the same indicating, that both can be used to correct the measured winds.

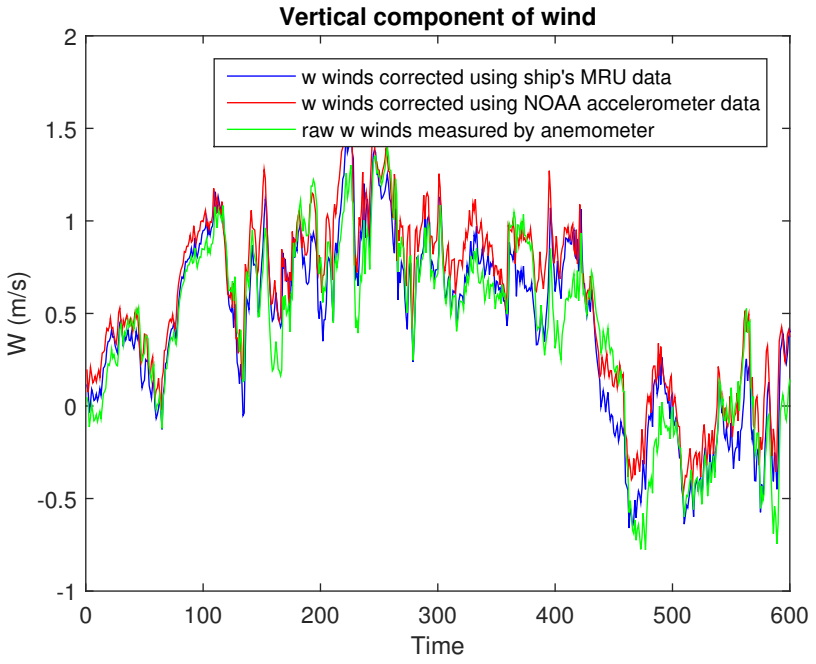

FIGURE 2.4: *Time series of the measured raw vertical wind speed by the anemometer (green), corrected vertical wind using ship's MRU data (blue), corrected vertical wind using NOAA accelerometer data (red).*

The time-averaged fluxes are calculated by using:

$$\tau = -\rho[i\overline{u'w'} + j\overline{v'w'}] \tag{2.6}$$

where ρ is the density of the air, the overline represents a time average, and u', v', w' are longitudinal, lateral and vertical velocity deviations from the mean. The stress τ computed using equation 2.6 has both the longitudinal and lateral components of stress. The vertical corrected velocity can be correlated with the scalar quantities to compute their vertical fluxes. The sensible(H), latent (E) and gas fluxes (F_c) can be calculated by:

$$H = \rho c_p \overline{w'\theta'} \tag{2.7}$$

$$E = \rho L_e \overline{w'q'} \tag{2.8}$$

$$F_c = \rho \overline{w'c'} \tag{2.9}$$

where θ', q', c' are the perturbations in the potential temperature, specific humidity and concentration of the gas measured respectively at high frequency. The heat and momentum fluxes are calculated using a 10-minute averaging period.

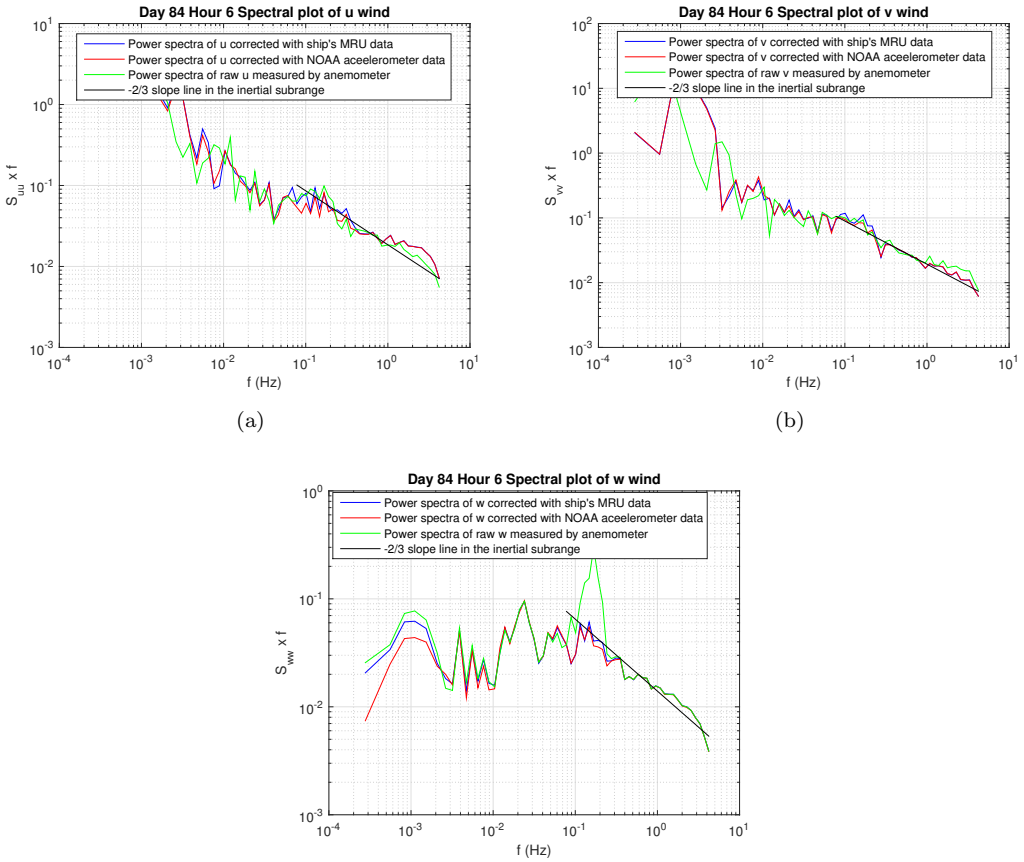

FIGURE 2.5: *Velocity power spectrum of the measured raw winds, winds corrected by ship's MRU data, and winds corrected by NOAA accelerometer data. The black straight line in the figure represents the expected -2/3 slope in the inertial sub-range.*

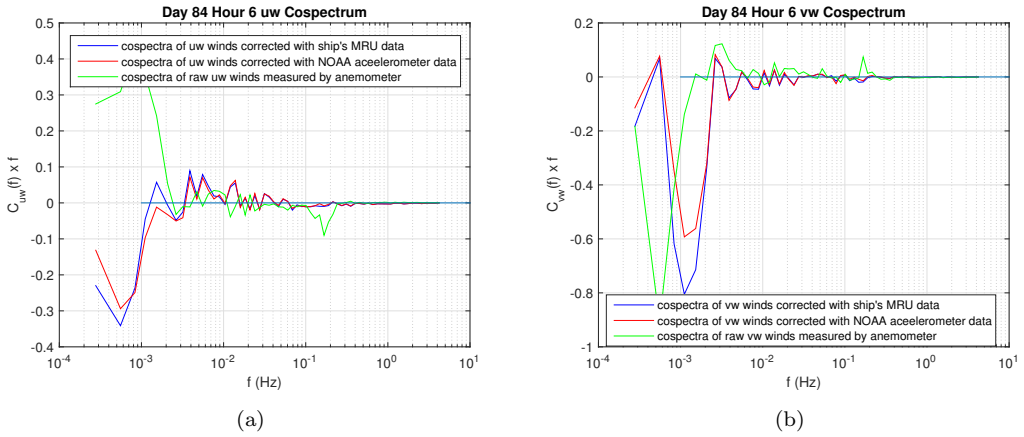

FIGURE 2.6: *Cospectrum for the measured raw winds (green), winds corrected by ship's MRU data (blue) and winds corrected by NOAA accelerometer data (red).*

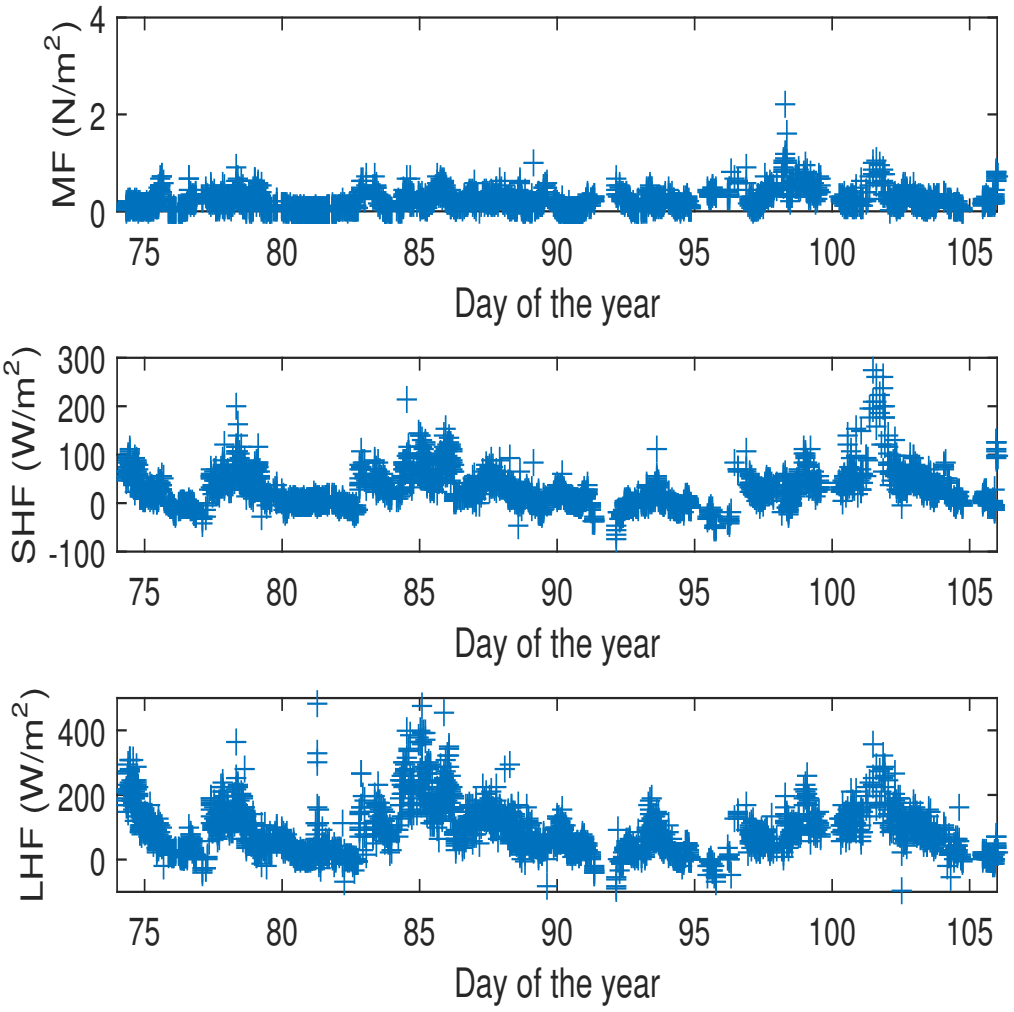

FIGURE 2.7: *Time series of the Momentum, Sensible heat and latent heat fluxes computed over 10 minute interval for entire CAPRICORN voyage.*

Figure 2.7 shows the time-series of the eddy co-variance estimates of momentum flux, sensible and latent heat fluxes.

With the use of the ship's MRU and navigation data, the platform velocities of the ship can be calculated. As the platform velocities of the ship can be calculated without the use of an external accelerometer, the accelerometer, heading sensor, and GPS receiver can be removed from the flux system. In this chapter, we have characterized that for the anemometer mounted on the foremast of the R/V Investigator, and there is a lag of 1.4 sec in the data measured by the ship's motion reference unit. It is seen that the spectral peaks (0.25 Hz) observed in the measured wind speeds by anemometer are

removed, thus successfully removing the platform motions from the measured winds, to make them useful to use in the eddy covariance.

Chapter 3

Momentum and Heat Fluxes

The turbulent fluxes computed by the eddy covariance technique after correcting the wind speeds for motion corrections, as discussed in Chapter 2, are used in this chapter to build a simple model to estimate the fluxes in terms of bulk non-dimensionless functions.

3.1 Turbulent Fluxes in Surface Layer

The turbulent fluxes that are calculated by the eddy covariance technique are to be applied to a series of screening procedures. The computed fluxes are discarded if:

- The standard deviation of relative wind direction is greater than 15^o.
- The standard deviation of the ship speed is higher than 0.6 m/s.
- The standard deviation of the heading is greater than 5^o.
- The tilt angle is greater than 10^o.
- The ship speed is more than 3.5 m/s.
- The rain rate is greater than 0 mm/hr.
- The relative wind direction with respect to the bow is not within the range of $\pm 60^o$.
- The standard deviation in platform velocity is greater than 0.8.

- The missing sonic data is greater than 50 in 10 min interval.

After quality control, the wind stress varies between $0.0008\,N/m^2$ to $1.04\,N/m^2$ for calculated U wind speeds varying between $0.6\,m/s$ and $17.2\,m/s$. The turbulent sensible and latent heat flux varies between -25 $\mathrm{W/m^2}$ and 140 $\mathrm{W/m^2}$, -38 $\mathrm{W/m^2}$ and 300 $\mathrm{W/m^2}$ for temperature difference ranging between 6.9 °K and -2.7 °K and humidity difference ranging between 0.0079 kg/kg and -0.0012 kg/kg. The total heat flux varies between 374 $\mathrm{W/m^2}$ and -7 $\mathrm{W/m^2}$.

Figure 3.1 shows the variation of turbulent fluxes of momentum, sensible and latent heat fluxes with wind speeds the color bar represents the temperature difference between the surface temperature and air temperature. It is seen that the fluxes depend on the velocity of the winds and the temperature difference between the ocean and air. This dependence is used to parameterize the fluxes in terms of non-dimensionless velocity and stability functions in section 3.2.

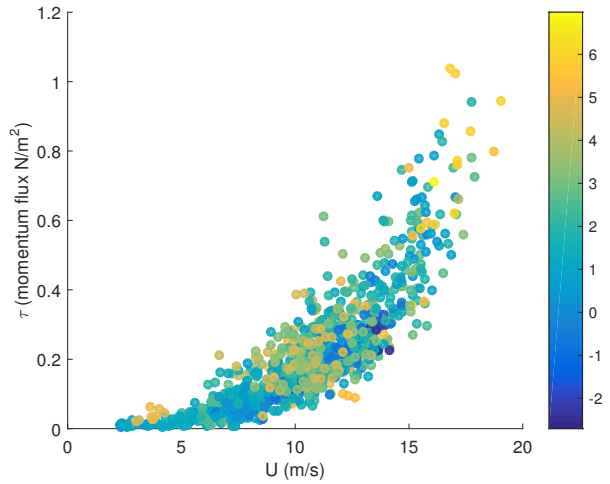

(a)

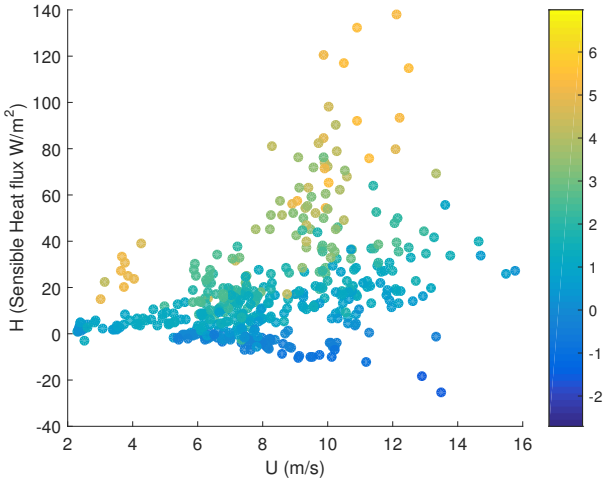

(b)

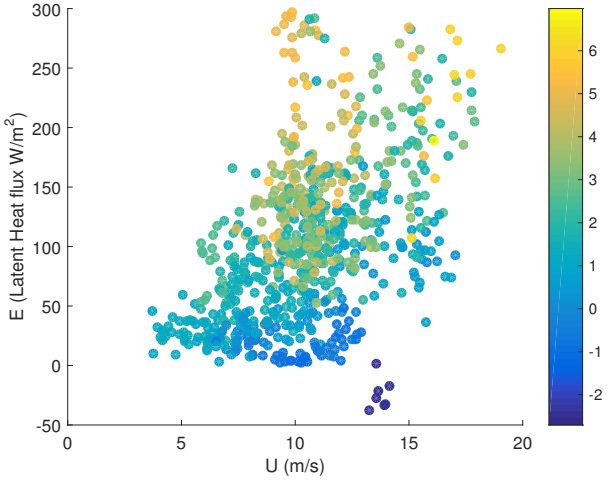

(c)

FIGURE 3.1: *Computed momentum flux, sensible, and latent heat fluxes variation with wind speed after applying all corrections. The color bar represents the temperature difference between the ocean surface and the air temperature.*

3.1.1 Comparison of turbulent fluxes with fluxes obtained from various bulk methods

Only the COARE bulk model parameterization has been validated against field observations in the Southern Ocean for the Southern Ocean Gas Experiment (GasEx) and CAPRICORN (Jackson et al., 2012; Bharti et al., 2019) observations. Here, the turbulent flux measurements that are computed using quality-controlled eddy covariance data from chapter 2 are compared with the fluxes estimated by inertial dissipation (ID) method, fluxes estimated using bulk model outputs from COARE (Coupled Ocean-Atmosphere Response Experiment) 3.5 model (Bariteau et al., 2018), RegCM (Regional Climate Model) and ECMWF IFS (European Centre for Medium-Range Weather Forecasts Integrated Forecast Systems) model. The equations and descriptions of the bulk model representations are given in Appendix A.1. Table 3.1 summarizes the flux comparisons of the turbulent measurements done on the R/V Investigator with the fluxes computed by the inertial dissipation method and bulk models using the bulk measurements done on the ship.

		ID	**COARE 3.5**	**RegCM**	**ECMWF IFS**
τ (N/m^2)	Mean	0.2082	0.1917	0.1857	0.2015
	Bias	0.0017	-0.0148	-0.0209	-0.0051
	RMSE	0.067	0.075	0.0818	0.0759
	r^2	0.8321	0.7891	0.7496	0.7844
	Uncertainty	32.157	39.1391	44.0291	37.6615
	MAE	0.0469	0.0503	0.0532	0.0519
SH (W/m^2)	Mean	18.9298	15.1221	17.7463	16.8577
	Bias	-0.9308	-4.7385	-2.1143	-3.0029
	RMSE	10.7734	11.7956	10.2904	10.7007
	r^2	0.8071	0.7687	0.8240	0.8097
	Uncertainty	56.9125	78.002	57.9862	63.4768
	MAE	7.4356	7.6493	6.8940	7.0146
LH (W/m^2)	Mean	129.4545	111.1346	122.3906	120.9502
	Bias	20.3401	3.7433	14.9993	13.5590
	RMSE	41.9264	33.4494	38.6847	37.8296
	r^2	0.6111	0.7580	0.6764	0.6905
	Uncertainty	32.387	30.0981	31.6076	31.2770
	MAE	30.3272	24.3747	27.8128	27.1684

TABLE 3.1: Error statistics for 10 minute turbulent fluxes as measured by eddy covariance with inertial dissipation (ID) method, COARE 3.3 model, RegCM model, ECMWF IFS model outputs calculated using the in-situ measurements. The uncertainity is calculated as RMSE $\times$100/Average and the negative sign indicates that the modeled values are less than the measured values.

The mean momentum, sensible heat, and latent for 10-minute fluxes obtained by eddy covariance estimates from the CAPRICORN voyage are 0.2066 $\mathrm{N/m^2}$, 18.491 $\mathrm{W/m^2}$ and 109.1144 $\mathrm{W/m^2}$ respectively. We can see that the Latent heat fluxes are more compared to the sensible heat fluxes over the oceans. From Table 3.1, it is seen that there is a clear high bias in the latent heat flux estimates through the ID method compared to that of eddy covariance estimates and bulk models when the bias is calculated with respect to the fluxes calculated by the eddy covariance. It is seen that among the bulk models, COARE 3.5 model is performing better compared to the other models for momentum and latent heat fluxes. For sensible heat fluxes, it is seen that the uncertainty is higher for all the estimates. Overall, we can say that the COARE 3.5 model is performing well

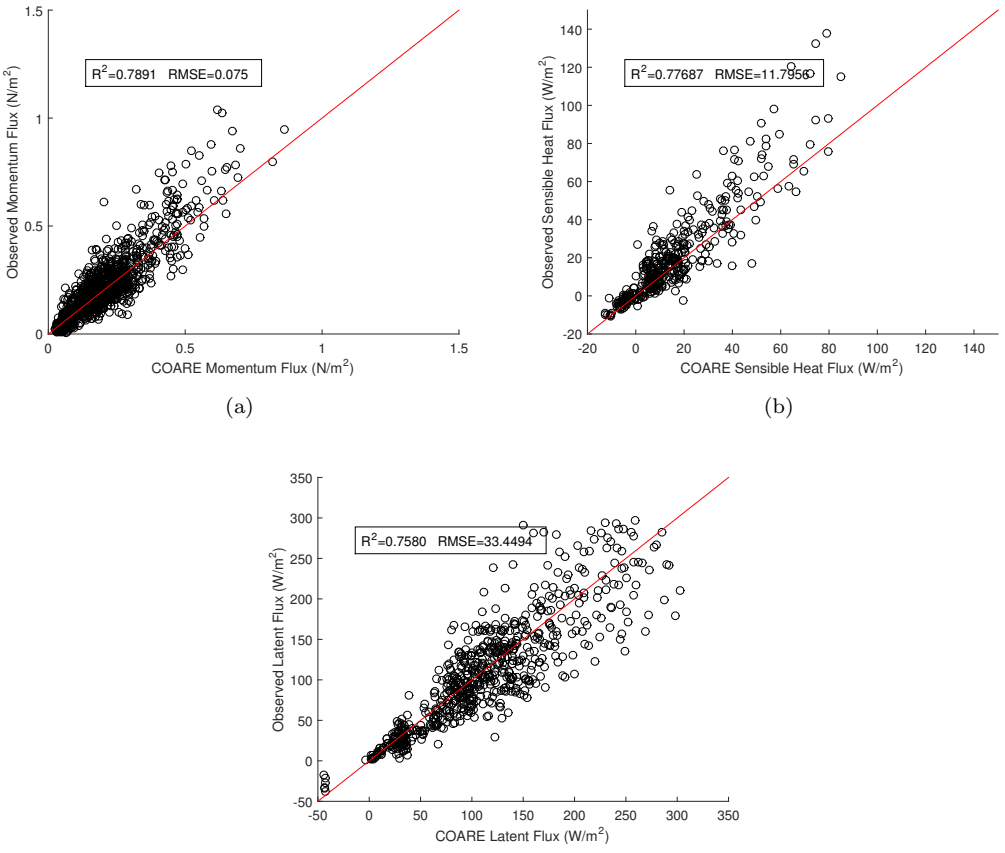

FIGURE 3.2: *Scatter plot of wind stress, sensible heat and latent heat fluxes computed from eddy covariance and COARE 3.5 bulk model.*

for momentum and latent heat fluxes compared to other methods, while the RegCM is performing better for the sensible heat flux. Figure 3.2 shows the scatter plot of the fluxes obtained from the direct eddy covariance technique and the COARE 3.5 bulk parameterization method. From the scatter plots, we can observe that at the higher wind speeds, the Eddy covariance estimates are higher compared to that of the COARE 3.5 model. The bulk models, when applied in the climate and NWP, underestimate the fluxes, which will affect the weather and climate.

3.1.2 Evaluation of transfer coefficients

The momentum, sensible and latent heat fluxes are parameterized in terms of bulk meteorological variables and the transfer coefficients. Several researchers have given the transfer coefficients for momentum as a function of wind speeds, and few of them gave transfer coefficients of heat as a constant. So, it is important for us to calculate the

transfer coefficients and see if the observed values are within the range of the previously observed values. The transfer coefficients of exchange are given as

$$C_D = \frac{\tau}{\rho U^2} \tag{3.1}$$

$$C_H = \frac{H}{\rho c_p \Delta\theta} \tag{3.2}$$

$$C_E = \frac{E}{\rho L_e \Delta q} \tag{3.3}$$

where, τ, H, E are the turbulent momentum, sensible heat, and latent heat fluxes respectively, ρ is the density of air, $\Delta\theta$ and Δq are the virtual temperature and specific humidity differences between the surface and at the measurement height. Figure 3.3 shows the calculated turbulent transfer coefficients with wind speeds. The drag coefficients varied between 1.0255e-04 and 0.0051 for wind speeds 2 and 20 m/s, while sensible heat and latent heat transfer coefficients varied between 0.005 and -0.0037, and 0.0034 and 1.3966e-04 respectively. From figures 3.3(a) - 3.3(c), it is seen that the momentum, sensible and latent heat transfer coefficients decreased with the wind speed in the low-speed regime, and the momentum and sensible heat transfer coefficients increased with wind speeds over 5 m/s.

Several studies were performed over the past few decades to calculate the turbulent transfer coefficients. The number of studies to calculate the drag coefficients are relatively large compared to studies that calculated the sensible and latent heat transfer coefficients. Studies have shown that the neutral drag coefficient is a function of wind speed ((Smith, 1980; Wu, 1980; Large and Pond, 1981; Garratt, 1977; Petersen and Renfrew, 2009; Andreas et al., 2012; Bumke et al., 2014; Yelland and Taylor, 1996; Smith et al., 1992; Geernaert et al., 1986)). Recent studies have shown that the coefficient is reduced or is constant at wind speeds above 30 m/s ((Powell et al., 2003; Donelan et al., 2004; Jarosz et al., 2007; Holthuijsen et al., 2012; Donelan, 2018)).

Neutral coefficients are to be computed to compare the results from the current study to previous studies. For neutral coefficients, the data has to be separated into neutral, unstable, and stable regimes from the entire data.

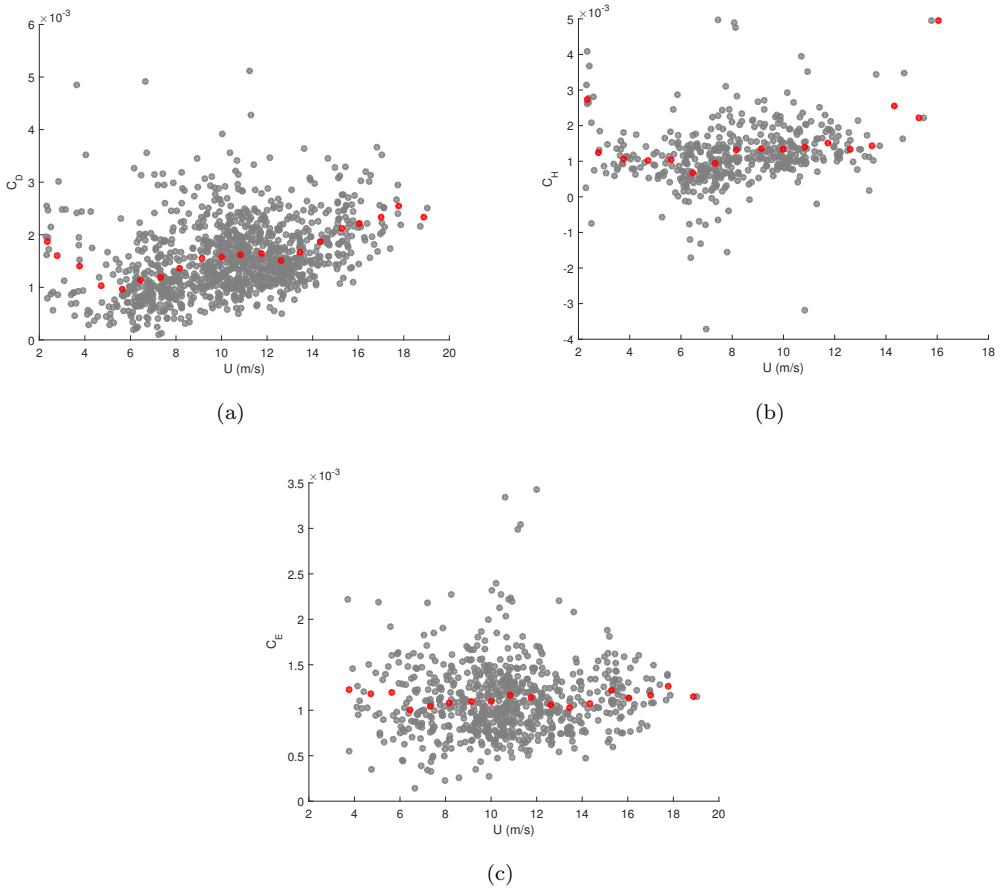

FIGURE 3.3: *Computed momentum, sensible and latent heat flux transfer coefficients with wind speeds after all corrections.*

Bulk Richardson number, is the dimensionless number, which is the ratio of the buoyancy production term and the shear production term. Bulk Richardson number is given by equation 3.4, where $\theta_v = \theta(1 + 0.61q)$ is the virtual potential temperature at height z and g is the acceleration due to gravity. Here, the bulk Richardson number is used to classify the boundary layer into stable, neutral, and unstable cases. The classification used in this study is as follows:

- Unstable - $R_b < -0.002$
- Neutral - $-0.002 < R_b < 0.002$
- Stable - $R_b > 0.002$

$$R_b = \frac{(\theta_v - \theta_{v0})gz}{\theta_v U^2} \tag{3.4}$$

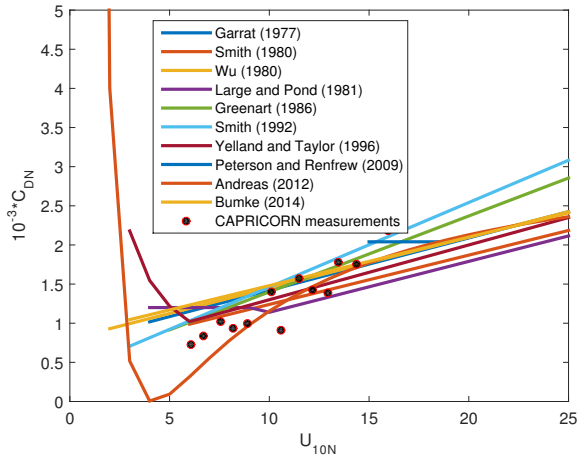

FIGURE 3.4: *Parameterizations of C_{DN} as a function of wind speed proposed in various studies, black dots represent the neutral drag coefficients from the present study where only data during near neutral conditions are used and binned over the wind speeds, where the 10m wind speeds are calculated using the logarithmic approximation.*

Figure 3.4 shows the neutral drag coefficients given by different studies; black dots are the neutral drag coefficients calculated in the present study binned over wind speeds. The results are very well within the range of previous studies. Figure 3.5 show the neutral exchange coefficients of momentum, sensible and latent heat fluxes with wind speeds at 10 m, where the wind speeds are calculated using the logarithmic approximation. The neutral exchange coefficients of sensible and latent heat are less reported than that compared to the drag coefficients due to lack of measurements (Drennan et al., 2007). Most studies suggest that the neutral coefficients do not depend on wind speed and are nearly constant with wind speed in the moderate wind speed regime (Large and Pond, 1982; DeCosmo et al., 1996; Persson et al., 2005; Cook and Renfrew, 2015; Zou et al., 2017). Even at high wind speeds, where wave breaking and sea spray are believed to be important in air-sea exchange, wind speed dependence is not evident (Zhang et al., 2008; Cook and Renfrew, 2015; Petersen and Renfrew, 2009).

Experimental studies were conducted to calculate the fluxes, and the computed fluxes are used to parameterize the fluxes in terms of the bulk meteorological values so that they can be used in the NWP and climate models. Most parameterizations use MOST and Charnock's relations to calculate the transfer coefficients. These parameterizations are iterative hence giving rise to circular dependencies. Therefore, a simple parameterization is proposed here, which is simple and does not depend on any assumptions, which is described in section 3.2.

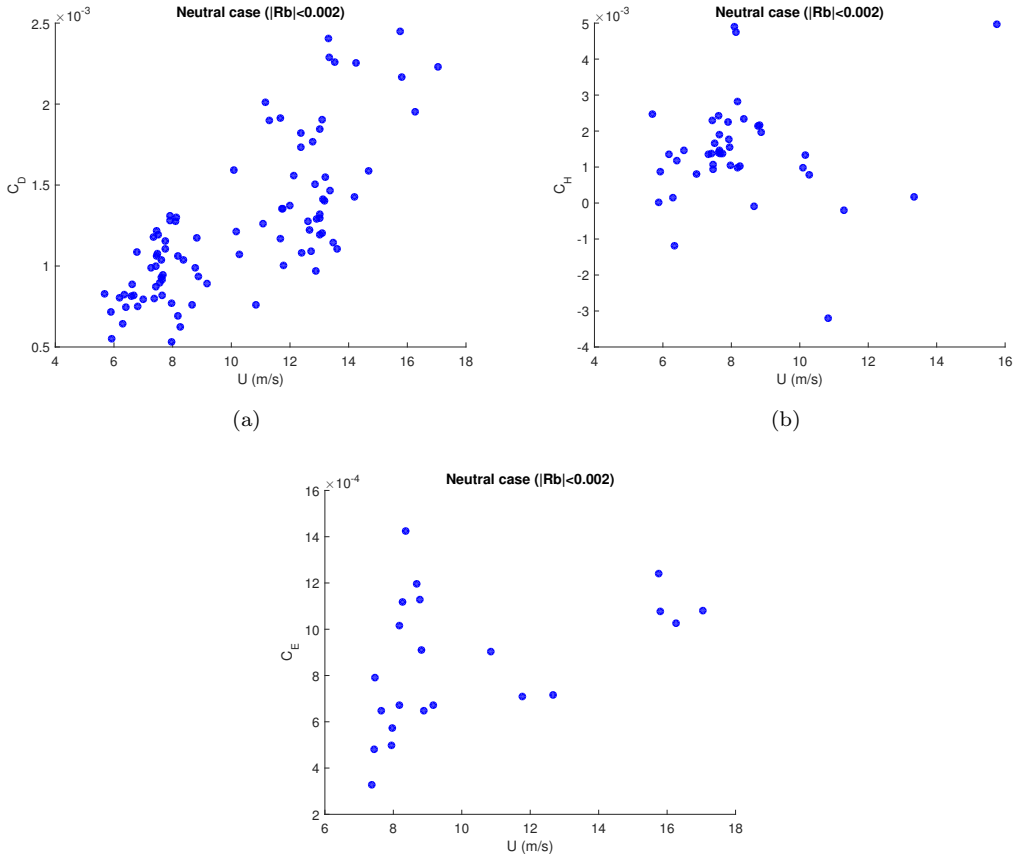

FIGURE 3.5: *Computed momentum, sensible and latent heat flux neutral transfer coefficients with wind speeds at 21 m height, after all corrections.*

3.2 Parameterization of fluxes in terms of velocity and stability functions

Momentum, sensible and latent heat fluxes in numerical weather prediction and climate models are parameterized using bulk algorithms. The momentum and heat fluxes in these models are given by equations 3.5-3.7 where the C_D, C_H, C_E are the dimensionless coefficients that depend on MOST and Charnock's relations.

$$\tau = \rho_a C_D U^2 \tag{3.5}$$

$$H = \rho_a C_H c_p \Delta\theta \tag{3.6}$$

$$E = \rho_a C_E L_e \Delta q \tag{3.7}$$

The physical interpretation of MOST can be ambiguous due to self-correlation and circular dependence (Vickers et al., 2015) as MOST employs an iterative process to predict turbulent fluxes in terms of exchange coefficients that depend on stability functions and thus on turbulent fluxes through Obukhov length. In order to avoid the iterative process, Kara et al. (2005) has formulated the exchange coefficients obtained from the COARE algorithm as functions of wind speed, temperature, and humidity. Vickers et al. (2015) and Zou et al. (2017) has modeled the friction velocity and exchange coefficients as a function of velocity and bulk Richardson number and Richardson numbers, respectively.

Zou et al. (2017) defined Richardson number, which does not depend on measurement height and assumes that u_*, q_*, θ_* and z_0 are constant with height in the atmospheric boundary and is given as

$$R_i = 3 \times 10^4 \alpha \theta_{v*} / \theta \tag{3.8}$$

where α is the Charnock constant, $\theta_{v*} = \theta(1 + 0.61 q_*)$.

Vickers et al. (2015), in their study, parameterized the fluxes in terms of velocity and stability functions, where they used bulk Richardson number as the stability parameter. The bulk Richardson number is given by equation 3.4.

Though the bulk Richardson number depends on the measurement height, it does not require the MOST iterative process to determine the fluxes, while Richardson's number requires the scaling temperature, which requires the turbulent measurements hence cant be used to determine the fluxes through the mean meteorological data. In this study, we parameterize the fluxes using the functions of bulk Richardson number as used by Vickers et al. (2015) and roughness Reynolds numbers to make them dimensionally stable and non-iterative. The roughness Reynolds number used hereafter in this paper is defined as

$$R_e = zU/\nu \tag{3.9}$$

where z is the measurement height, U is the wind speed and ν is the kinematic viscosity of the air.

Here, following Vickers et al. (2015), we formulate the momentum, sensible and latent heat fluxes as functions of non-dimensionless numbers as shown below.

$$\tau = \rho U^2 f_{mf}(R_e) h_{mf}(R_b) \tag{3.10}$$

$$SHF = \rho c_p U \Delta\theta f_{shf}(R_e) h_{shf}(R_b) \tag{3.11}$$

$$LHF = \rho L_e U \Delta q f_{lhf}(Re) h_{lhf}(R_b) \tag{3.12}$$

In this simple model, as stated by Vickers et al. (2015), the measured wind speed is not adjusted based on height or stability, unlike in MOST. It also states that the model minus measurements residuals for u_* by measurement height are near zero for low measurement heights. Also, these are positive for higher measurement heights, which are consistent with an underestimate of the observed values, whereas the COARE model u_* residuals are near zero for low measurement heights and negative for the measurement heights exceeding 30 m. Thus we can expect a strong height dependence in this model, and we can use it as the COARE model yields a stronger height dependence.

To obtain function $f(R_e)$, we follow the process as followed by Vickers et al. (2015), we examine the dependence of $\tau/\rho U^2$, $SHF/\rho U c_p \Delta\theta$, $LHF/\rho L_e U \Delta q$ with R_e in near-neutral cases, where we considered the magnitude of R_b is less than 0.002, where $h(R_b)$ is expected to be unity, considering the data above above 5 m/s. The functions, $f(R_e)$ are found by fitting the data. It is seen that for sensible heat flux, there is no dependence of flux coefficient with the Reynolds number, hence in this study, we do not give any parameterization for the sensible heat flux. In ideal neutral conditions, the sensible heat flux across the interface has to be zero, however in the real world observations, there would be values near to zero, however, the sensible heat flux coefficients does not depend on any wind speed or temperature difference in this stability zone. Hence it would be difficult to get a parameterization, which is a function of non-dimensionless velocity and stability functions.

$$f(R_e)_{mf} = 6.481 * 10^{-11} * R_e + 0.0001195 \tag{3.13}$$

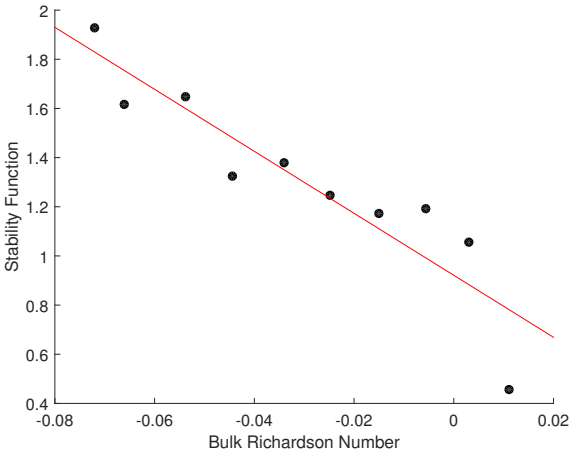

FIGURE 3.6: *Stability function versus Richardson number for latent heat flux.*

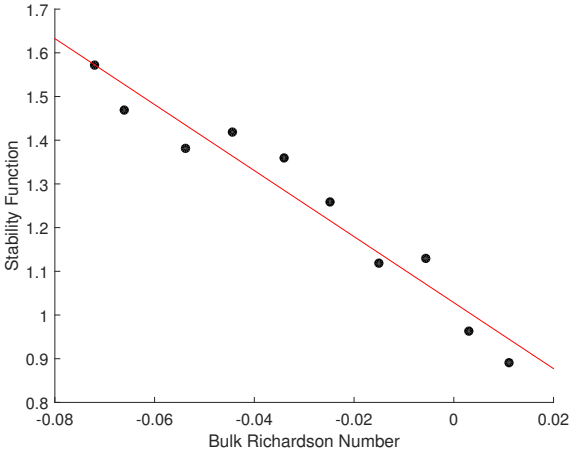

FIGURE 3.7: *Stability function versus Richardson number for momentum flux.*

$$f(R_e)_{lhf} = 1.308 * 10^{-11} * R_e + 0.0007594 \tag{3.14}$$

The bulk stability functions are obtained by fitting the data between the Richardson number and bin mean-ed data of $\tau/\rho U^2/f(R_e)_{mf}$ and $LHF/\rho L_e U \Delta q f(R_e)_{lhf}$

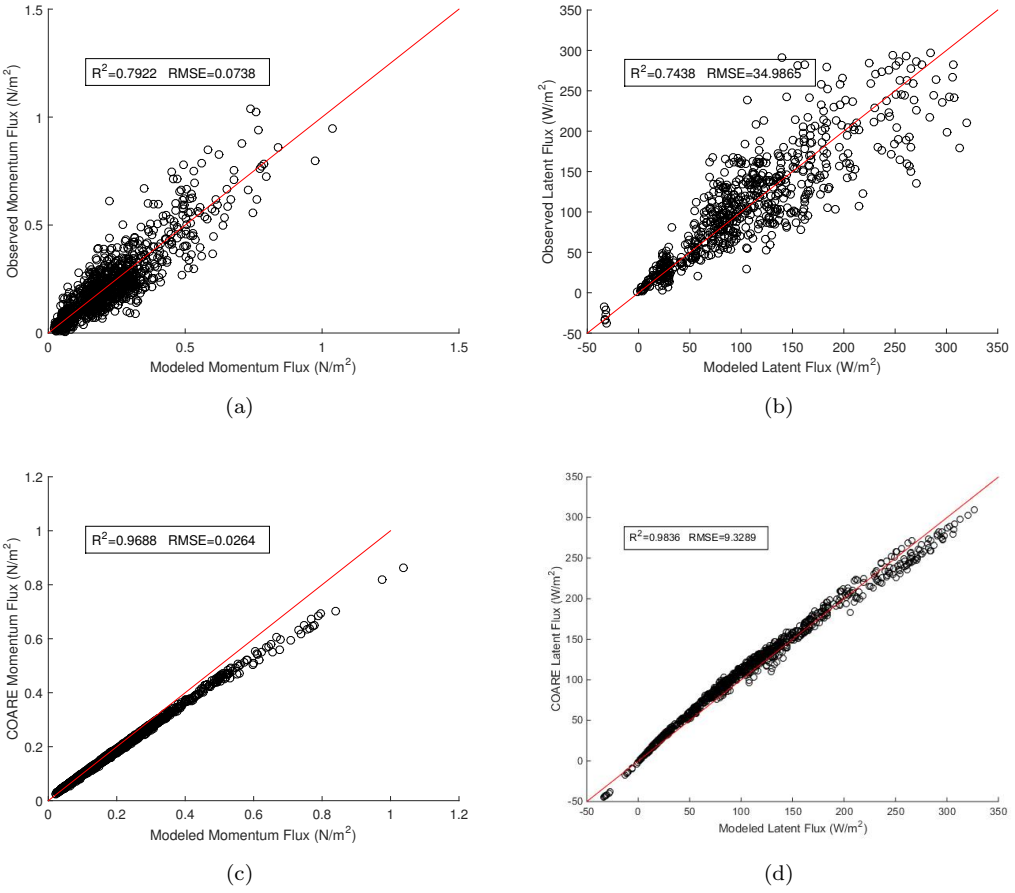

FIGURE 3.8: *Scatter plot of the observed fluxes with the simple modeled fluxes and (top) and scatter plot of the COARE modeled fluxes with the simple modeled fluxes (bottom).*

$$h(R_b)_{mf} = -7.526 * R_b + 1.029 \tag{3.15}$$

$$h(R_b)_{lhf} = -9.194 * R_b + 0.8025 \tag{3.16}$$

Figures 3.7 and 3.6 show the stability function h_{R_b} with the Richardson number, the curve fitted represent the equations 3.15 and 3.16. To compare our simple model predictions of the fluxes to the observations and the COARE 3.5 model outputs, scatter plots are shown in figure 3.8. It is seen that the coefficient of determination, r^2 is as good as that compared to that of the COARE 3.5 model. From the scatter plot of the COARE 3.5 output and the simple model output, we can conclude that our fluxes computed at the high winds are better in the simple model than those from the COARE 3.5 model.

Chapter 4

CO_2 Fluxes

This chapter discusses how measurements of carbon dioxide are done in the atmosphere and water and what are the corrections done to calculate the carbon dioxide fluxes. It discusses the data processing required and how to calculate the gas transfer velocities and convert them to a Schmidt number of 660.

4.1 Observations

An open path LICOR 7500 infrared gas analyzer is used for CO_2 flux measurements. LICOR 7500 is designed to measure high-speed CO_2 and H_2O concentration in ambient air. It has a calibration range of 0-3000μmol mol^{-1} for CO_2 and 0-60 mmol mol^{-1} for H_2O, with an accuracy of 1% of the measured value.

The partial pressure of CO_2 in water is obtained from the underway measurements of CO_2 done on the surface seawater by using a General Oceanics/Neill system that is equipped with a shower head equilibrator and uses a nondispersive infrared gas analyzer (LICOR, LI7000) to quantify the CO_2 in gas circulated from equilibrator headspace and dried prior to measurement using a Nafion Dryer. The accuracy and precision of the measurements are ± 2 μatm (Moreau et al., 2017). The observations were made at a frequency of 0.2 Hz. The measured CO_2 concentrations are not quality controlled. Hence a series of checks are performed, and unrealistic values are removed.

4.1.1 Dilution Corrections

The open path LICOR 7500 gas analyzer measures the concentration of carbon dioxide in the moist air. Hence, we need to correct the measured raw concentrations to account for these dilution effects (Webb et al., 1980) before computing the fluxes. The method we used here to correct for dilution effects is similar to the one used by Edson et al. (2011), where the approach is to "dry" the samples numerically by applying an additional dilution correction to estimate the mixing ratio. The mixing ratio,r_c is given as,

$$r_c = \frac{RT}{MP}\frac{\chi_c}{(1-q)} \tag{4.1}$$

where χ_c is the mass concentration of carbon dioxide, typically observed by the LICOR 7500 gas analyzer, R is the ideal gas constant, T is the temperature, P is the pressure, M is the molecular weight of the moist air, q is the specific humidity.

4.2 Gas transfer velocity calculation

The gas transfer velocity k is given by equation 4.2

$$k = \frac{F_c}{\Delta pCO_2} \tag{4.2}$$

where F_c is the turbulent gas flux computed using the eddy covariance technique and ΔpCO_2 is the concentration difference across the air-water interface.

The $p\mathrm{CO}_2$ of water obtained from the ship and the CO_2 concentrations measured from LICOR are averaged to 10-minute data. Figure 4.1 shows the measured concentration CO_2 in the air and water. However, we see that the concentration of carbon dioxide in water is more in some places compared to that of the air. However, the literature suggests that the Southern Ocean as the sink of carbon dioxide and the concentration of carbon dioxide is less in water. Eddy covariance measurements to compute fluxes in the Southern Ocean were done in the past during the SO-Gas Experiment (Edson et al., 2011) and SOAP Experiment (Landwehr et al., 2014). It is seen from both the studies that the concentration of carbon dioxide in water is less compared to that in the air.

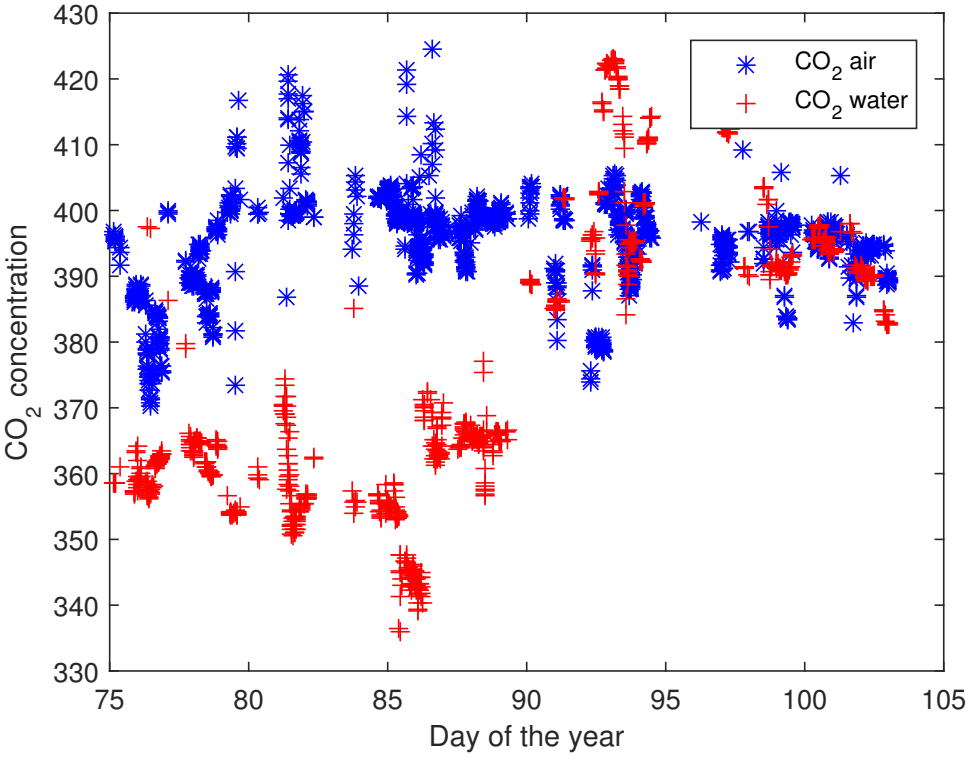

FIGURE 4.1: *CAPRICORN time series data of CO_2 (ppm) concentration in air and water. The data is averaged over 10 minute intervals.*

The gas transfer is calculated only when the difference in concentration in air and water is chosen to be less than 40, following the previous studies.

The carbon dioxide concentrations of air and water are filtered for the rate of change in a mean concentration greater than 5ppm per 10min. The filtered measurements are used to calculate the concentration difference across the interface.

The turbulent fluxes of carbon dioxide are computed following the procedure followed to calculate the fluxes of heat as that computed in the chapter 2. The streamwise and cross-stream covariance, along with the vertical component, are calculated. The computed fluxes are filtered for all the quality checks that are listed in Chapter 2. The fluxes are also filtered if the streamwise and cross streamwise fluxes of the gas are greater than 0.06 ppm m/s (Blomquist et al. (2017)). The gas transfer velocity is thus computed using equation 4.2 after all the criteria are fulfilled. The computed gas transfer velocities are normalised to a Schmidt number of 660, which corresponds to CO_2 at 25^oC by using

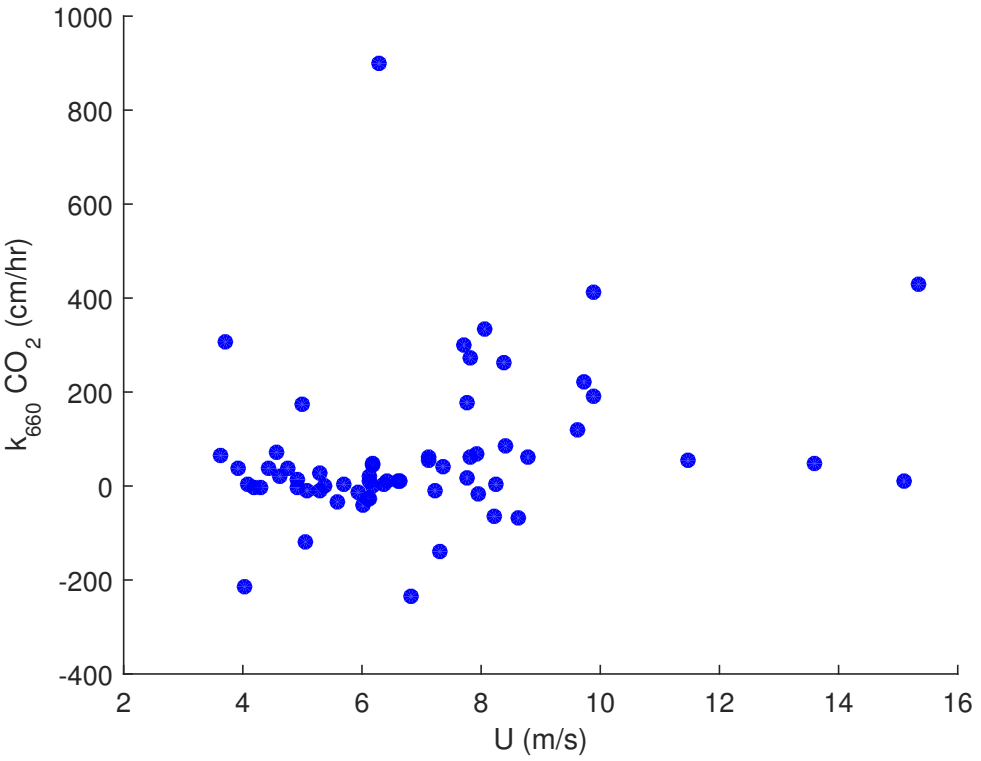

FIGURE 4.2: *Measured values of gas transfer velocity from the CAPRICORN data.*

equation 4.3.

$$k_{660} = k\sqrt{\frac{Sc_{CO_2}}{660}} \tag{4.3}$$

where Sc is the Schmidt number, which is a function of sea surface temperature, Ts ((Wanninkhof, 1992)).

$$Sc = 2073.1 - 125.62 * Ts + 3.6276 * Ts^2 - 0.043219 * Ts^3 \tag{4.4}$$

4.3 Wind Speed Dependence

Several studies reported the dependency of gas transfer velocity on wind speed. These gas parameterizations proposed were based on field and laboratory experiments, ranging from a linear relationship to quadratic, cubic, or power-law with wind speeds.

Figure 4.2 shows the wind speed dependence on gas transfer velocity for the CAPRICORN data. Very few data points are achieved after proper quality control of the data. Hence, it would be difficult to give a proper relationship of gas transfer velocity with the

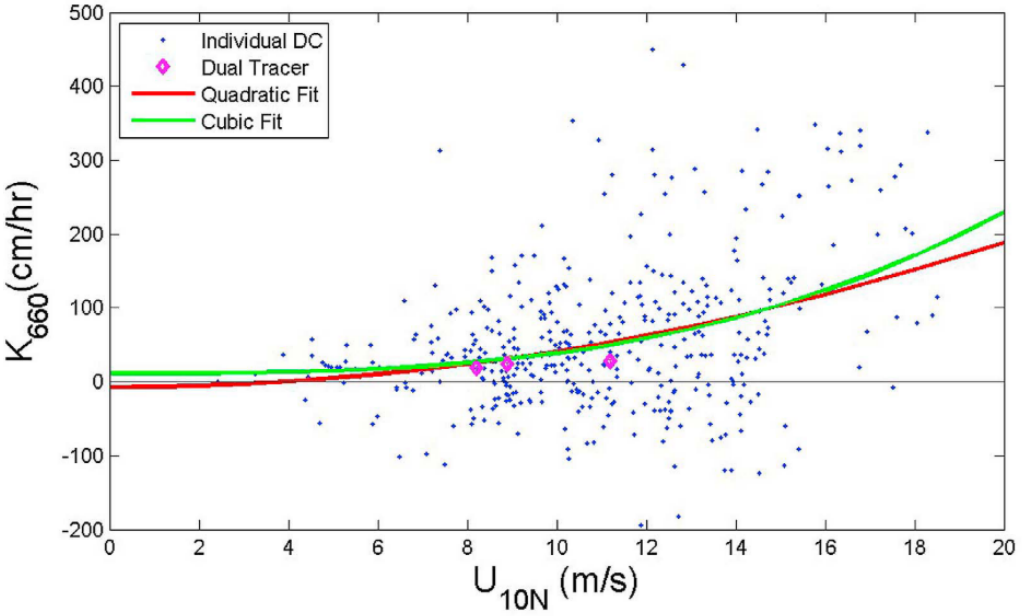

FIGURE 4.3: *Measured values of gas transfer velocities from SO GasEx showing a quadratic and a cubic fit.*

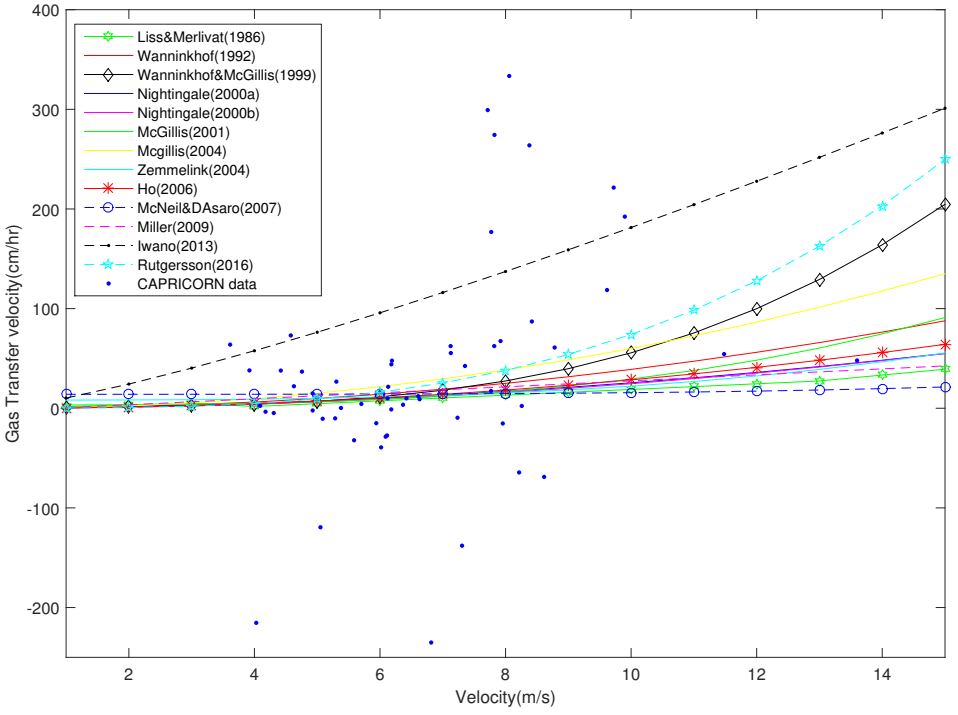

FIGURE 4.4: *Measured values of gas transfer velocities from CAPRICORN data (blue dots) overlayed over the parameterizations given by different researchers.*

wind speeds. However, if we consider the single data point whose gas transfer velocity is greater than 500 cm/hr as an outlier, remaining data points are within the observed ranges from the previous studies. The maximum gas transfer velocity values reported in the literature to date is during the SO-Gas Experiment. The values reported varied between 500 and -200 cm/hr (Edson et al., 2011) for wind speeds between 0 and 20 m/s. Figure 4.4 shows the calculated values of gas transfer velocity of carbon dioxide in the Southern Ocean during the CAPRICORN voyage overlayed over the relationship's given by other researchers. The figure 4.3 shows the spread of the gas transfer velocities observed during the Southern Ocean Gas Experiment obtained from the eddy covariance estimates. The authors have given least-squares fit the data They have given a linear, quadratic, and a cubic fit to the data. The coefficients of determination for these fits for the individual eddy covariance estimates are 0.1, 0.112, and 0.118, respectively, while the coefficient of determination for the equally spaced wind speed binned data is 0.789, 0.872 and 0.893 for linear, quadratic and cubic relations. It was concluded that a cubic relationship provides an accurate parameterization for the gas transfer velocity. Landwehr et al. (2018) has given the dependence of gas transfer velocities on the friction velocity observed in the Southern Ocean Aerosol Production Experiment. The coefficient of determination observed for a linear fit with the eddy covariance estimates and friction velocity is 0.35. Hence from the literature, we can see that there is a vast spread in the data measured, enhancing the need to have more observations in this region. Although researchers have studied the dependence of gas transfer velocity with the breaking wave parameter, mean root square of wave slope, white capping coverage area, bubble concentration, wind speed dependence is more extensively studied. As the literature suggests that the gas transfer velocities observed at high wind speeds are greater, we need to have more observations in the high wind speed region to have a more robust and reliable equation. A more robust and reliable equation is necessary to estimate the ocean sink of carbon dioxide accurately.

Chapter 5

Conclusion

The Earth is an integrated system consisting of four subsystems, namely atmosphere, hydrosphere, lithosphere, and biosphere. These subsystems interact and influence each other. The interactions between these subsystems occur through the exchange of mass and energy. And the rate of movement of these across the systems is termed as fluxes. These interactions have an important influence on the understanding of weather and climate of the earth system. Air-sea interactions are one such interaction that influences the Earth's environment making it important to understand the physical processes influencing weather and climate prediction and forecasting. Thus, calculating fluxes and understanding the physical processes that affect the fluxes across the air-sea more important. Various studies were performed to understand the processes that affect the fluxes, and the influence of stability on the fluxes is less studied. Various researchers have given the fluxes in terms of bulk variables and transfer coefficients. Few studies gave the transfer coefficients as a function of wind speeds, which are dimensionally not stable, while a few of them gave them as a constant, and few of them used MOST and Charnock's relations to give the transfer coefficients. The current state-of-the-art climate and weather prediction models use bulk models based on the MOST and the Charnock's relationships to determine the fluxes across the air-sea interface, which is an iterative process. These bulk models depending on MOST, have circular dependencies. The COARE 3.5 model is the best performing model available, and it is seen that at higher wind speeds, the COARE model underestimates the fluxes when compared with the measurements that obtained from the CAPRICORN experiments. Therefore, we

need to build a simple parameterization of flux coefficients to determine fluxes to avoid assumptions and circular dependencies and which is dimensionally stable.

Eddy Covariance is the purest form of flux calculation. The fluxes in a box can be estimated by measuring how many parcels of air with pass through a defined volume over a specific time. The Eddy covariance relies on high-frequency 3-D winds and the entity of interest. The eddy flux computed is proportional to the covariance of the fluctuation of the vertical wind from the mean and the deviation of the measured entity from the mean. The wind speeds, when measured on ships, are contaminated by the platform motions. However, the calculation of these motions is difficult in the absence of reliable accelerometer data or a failed collocated accelerometer. Here we investigated in this study whether the motion reference data of the ship can replace existing accelerometer collocated data. We characterized that for the anemometer mounted on the R / V Investigator's foremast, there is a lag of 1.4 sec in the ship's motion reference unit data. This lag can change based on the position vector of the motion reference unit and the anemometer; however, after characterizing the ship for different position vectors, we can use the ship's data to compute platform motions. Hence, we can correct the wind speeds for platform motions using the ships' motion data after adjusting to the lag. The spectral speaks due to the platform motions observed in the measured raw data by anemometer at 0.25 Hz is removed after the corrections performed by the ship's data. Therefore, the existing collocated accelerometer, GPS receiver, and heading sensors gain redundancy.

Momentum, sensible, and latent heat fluxes are computed using the motion-corrected winds by the eddy covariance method. A series of quality standards are applied to the fluxes. The quality controlled fluxes from the voyage are used to get a simple parameterization to estimate fluxes. The coefficients of momentum, sensible heat, and latent heat are calculated, and the results obtained are within the range of the observed values by the other researchers. In this study, we have developed the coefficients of momentum and latent heat fluxes in terms of simple functions of Reynolds and bulk Richardson number. Reynolds and bulk Richardson number are physically dependent on velocity and stability of the atmospheric boundary layer. The model proposed does not depend on any assumptions or does not have any circular dependencies and is dimensionally stable. The sensible heat flux coefficient could not be parameterized as we found that in the neutral region, there is no dependency on the Reynolds number. The proposed

model is performing better compared to that of the COARE 3.5 model at higher wind speeds.

Gas transfer across the air-sea interface is challenging to measure. It is essential to measure gas transfer velocities in the Southern Ocean as it is least sampled with the rough environment and high surface waves. It is estimated that the Southern Ocean is the largest sink of anthropogenic carbon dioxide, with about 40% of the total world ocean sink. Only two studies are reported in the Southern Ocean. Studies reported that the gas transfer velocity dependence on velocity, mean square slope of the waves, breaking wave parameter, and white capping area. Most of the studies suggested a high dependence on the velocity of winds. The existing relationships for the gas transfer velocity with wind speeds vary from linear to quadratic to cubic to a power law. From the existing parameterizations, it is seen that at the high wind speeds, there is high variance. CO_2 fluxes in the Southern Ocean are measured for the CAPRICORN voyage, using the motion-corrected winds and the measured concentrations of CO_2. After applying quality control to the calculated fluxes, gas transfer velocities are computed, and it is found that the results obtained are within the range that is reported by the previous researchers. However, there are no sufficient data points, and the variance in the data is too high to get any conclusions from the results obtained.

Measuring the gas transfer velocities at high wind speeds in the field is difficult. Hence, we can do experiments in the laboratory over a wind-wave tank where we can simulate the wind waves to calculate the gas transfer velocities. It is expected that the gas transfer velocities depend on the atmospheric stability. However, no study has reported the dependence of the gas transfer velocity on the stability of the atmosphere. Hence we can carefully design the experiments to get the gas transfer velocities for high wind speeds and different stability conditions.

Appendix A

Bulk Models

A.1 Introduction

The surface layer is a thin layer, which is typically about one-tenth of the Planetary Boundary Layer (PBL) height. The variables such as wind speed and potential temperatures and specific humidity experience the largest vertical gradients which are given by the surface layer similarity theory.

The surface layer fluxes are typically represented by bulk aerodynamic algorithms. These are given by the relationships of the MOST and the Charnock's relations. These depend on the momentum, temperature, and humidity roughness lengths and the stability functions. MOST is used in oceans as well as on land. Nevertheless, the lengths of roughness vary across the land and oceans, while the functions of stability remain constant across any surface. While surface fluxes and large environmental variables can be directly measured, parameterization is required for roughness lengths. Because the roughness lengths ' functional shape (or constant value) depends on the turbulent stability functions, different groups have suggested very different equations for roughness lengths. The surface layer schemes in the climate and weather model provide exchange coefficients for heat and momentum to the Ocean model, and friction velocities to the Planetary boundary layer computational modules. In essence, the Surface Layer schemes provide the parameterization linkage for the dynamic and thermal phenomena between ocean and atmosphere. Namely; it provides friction velocity and surface fluxes over oceans to PBL schemes.

A.1.1 RegCM3

Dimensionless vertical wind and scalar (temperature and humidity) gradients in the atmospheric surface layer can be defined as (Zeng et al. (1998)):

$$\phi_m = \frac{\kappa z}{u_*}\frac{du}{dz} \tag{A.1}$$

$$\phi_h = \frac{\kappa z}{\theta_{v*}}\frac{d\theta_v}{dz} \tag{A.2}$$

$$\phi_e = \frac{\kappa z}{q_*}\frac{dq}{dz} \tag{A.3}$$

where κ is the von karman constant(0.4), u is the wind speed, θ_v is the virtual potential temperature, u_* is the friction velocity, and θ_{v*} is the temperature scaling parameter. Using the Monin - Obukhov similarity theory, the flux - gradient relations are:

$$\phi_m = \phi_h = 1 + 5\zeta \tag{A.4}$$

under stable conditions (i.e., $\zeta > 0$) and

$$\begin{aligned} \phi_m &= (1 - 16\zeta)^{-1/4}, \\ \phi_h &= (1 - 16\zeta)^{-1/2} \end{aligned} \tag{A.5}$$

under unstable conditions (i.e., $\zeta < 0$). The dimensionless height ζ is defined as

$$\begin{aligned} \zeta &= \frac{z}{L}, \\ L &= \frac{\theta_v u_*^2}{\kappa g \theta_{v*}} \end{aligned} \tag{A.6}$$

is the Monin-Obukhov length. Under very unstable conditions, the flux gradients used are:

$$\begin{aligned} \phi_m &= 0.7\kappa^{2/3}(-\zeta)^{1/3} \\ \phi_h &= 0.9\kappa^{4/3}(-\zeta)^{-1/3} \end{aligned} \tag{A.7}$$

To ensure continuous functions of $\phi_m(\zeta)$ and $\phi_h(\zeta)$, the simplest approach is to match A.7 with A.5 at $\zeta_m = -1.574$ for $\phi_m(\zeta)$ and $\zeta_h = -0.465$ for $\phi_h(\zeta)$. Under very stable conditions,

$$\phi_m = \phi_h = 5 + \zeta \tag{A.8}$$

which matches 1.12 at $\zeta = 1$. The wind profiles are given as:

$$u(z) = \frac{u_*}{\kappa}\left(\left[ln\frac{\zeta_m L}{z_0} - \psi_m(\zeta_m)\right] + 1.14\left[(-\zeta)^{1/3} - (-\zeta_m)^{1/3}\right]\right) \tag{A.9}$$

for $\zeta < \zeta_m$ = -1.574;

$$u(z) = \frac{u_*}{\kappa}\left[ln\frac{z}{z_0} - \psi_m(\zeta)\right] \tag{A.10}$$

for $\zeta_m < \zeta < 0$;

$$u(z) = \frac{u_*}{\kappa}\left[ln\frac{z}{z_0} + 5\zeta\right] \tag{A.11}$$

for$0 < \zeta < 1$ and

$$u(z) = \frac{u_*}{\kappa}\left(\left[ln\frac{L}{z_0} + 5\right] + \left[5ln(\zeta) + (\zeta) - 1\right]\right) \tag{A.12}$$

for $\zeta > 1$. The potential temperature profiles are

$$\theta(z) - \theta_s = \frac{\theta}{\kappa}\left(\left[ln\frac{\zeta_h L}{z_{0t}} - \psi_h(\zeta_h)\right] + 0.8\left[(-\zeta_h)^{1/3} - (-\zeta)^{1/3}\right]\right) \tag{A.13}$$

for $\zeta < \zeta_h$ = -0.465;

$$\theta(z) - \theta_s = \frac{\theta_*}{\kappa}\left[ln\frac{z}{z_{0t}} - \psi_h(\zeta)\right] \tag{A.14}$$

for $\zeta_h < \zeta < 0$;

$$\theta(z) - \theta_s = \frac{\theta_*}{\kappa}\left[ln\frac{z}{z_{0t}} + 5\zeta\right] \tag{A.15}$$

for$0 < \zeta < 1$ and

$$\theta(z) - \theta_s = \frac{\theta_*}{\kappa}\left(\left[ln\frac{L}{z_{0t}} + 5\right] + \left[5ln(\zeta) + (\zeta) - 1\right]\right) \tag{A.16}$$

for $\zeta > 1$. Specific humidity profiles are same as they hold those forθ. The stability functions ψ_m and ψ_h are given as:

$$\begin{aligned}\psi_m &= 2ln\Big(\frac{1+x}{2}\Big) + ln\Big(\frac{1+x^2}{2}\Big) - 2\tan^{-1}(x) + \frac{\pi}{2}\\ \psi_h &= 2ln\Big(\frac{1+x^2}{2}\Big)\end{aligned} \tag{A.17}$$

where

$$x = (1 - 16\zeta)^{1/4} \tag{A.18}$$

θ_s is the surface potential temperature and q_s is the surface specific humidity over saline seawater, $q_s = 0.98 q_{sat}(T_s)$, where T_s is the sea surface skin temperature and q_{sat} is the saturation specific humidity for sea water at T_s. Under stable conditions, the wind speed u is defined as

$$u = max[(u_x^2 + u_y^2)^{1/2}, 0.1] \tag{A.19}$$

to avoid singularity at u=0, whereas for unstable conditions,

$$u = [u_x^2 + u_y^2 + (\beta w_*)^2]^{1/2} \tag{A.20}$$

to account for the the contribution of large eddies in the convective boundary layer to surface fluxes. u_x and u_y are mean wind components, and w_* is the convective velocity scale:

$$w_* = \left(- \frac{g}{\theta_v} \theta_{v*} u_* z_i \right)^{1/3} \tag{A.21}$$

where z_i is the convective boundary layer height which is taken as 1000 m, whereas β is taken as unity. Using the above equations, surface fluxes of momentum, sensible and latent heat can be obtained as

$$\tau = \rho u_*^2 (u_x^2 + u_y^2)^{1/2} / u \tag{A.22}$$

$$SH = -\rho C_p u_* \theta_* \tag{A.23}$$

$$LH = -\rho L_e u_* q_* \tag{A.24}$$

where ρ is the density of air, C_p is the specific heat of air, L_e is latent heat of vaporization. The ratio of $(u_x^2 + u_y^2)^{1/2}/u$ ensures the zero mean wind would result in zero wind stress. The roughness length of momentum (z_0) is given by:

$$z_0 = a_1 \frac{u_*^2}{g} + a_2 \frac{\nu}{u_*} \tag{A.25}$$

the roughness length of humidity and temperature are given as:

$$ln \frac{z_0}{z_{0q}} = b_1 Re_*^{1/4} + b_2$$
$$z_{0t} = z_{0q} \tag{A.26}$$

where $a_1 = 0.013, a_2 = 0.11, b_1 = 2.67, b_2 = -2.57$ are constants for observed wind speeds of 0.5 to 18 m/s, $Re_* = u_* z_0/\nu$ is the roughness Reynolds number, and ν is the kinematic viscosity of air. Using z_0 and z_{0q}, neutral exchange coefficients are computed.

$$\begin{aligned} C_{dn} &= \left(\kappa / ln\frac{10}{z_0}\right)^2 \\ C_{qn} &= \kappa^2/(ln\frac{10}{z_0} ln\frac{10}{z_{0q}}) \end{aligned} \tag{A.27}$$

A.1.2 Coupled Ocean - Atmosphere Response Experiment (COARE) 3.5

The turbulent transfer coefficients have a dependence on surface stability prescribed by MOST. The profile functions used in the free convection conditions are given by ((Fairall et al., 2003; Edson et al., 2013)):

$$y = (1-10.15\zeta)^{1/3}\psi_{uc} = 1.5log((1+y+y^2)/3) - \sqrt{3}tan^{-1}((1+2y)/\sqrt{3}) + \pi/\sqrt{3} \tag{A.28}$$

and

$$y = (1-34.15\zeta)^{1/3}\psi_{tc} = \psi_{qc} = 1.5log((1+y+y^2)/3) - \sqrt{3}tan^{-1}((1+2y)/\sqrt{3}) + \pi/\sqrt{3} \tag{A.29}$$

$$\psi_u = \frac{(1-f)\psi_{uk}}{f\psi_{uc}} \tag{A.30}$$

$$\psi_t = \psi_q == \frac{(1-f)\psi_{tk}}{f\psi_{tc}} \tag{A.31}$$

$$f = \frac{\psi^2}{(1+\psi^2)} \tag{A.32}$$

Under stable stratification, the profile equations used are

$$\psi_u = -\left[(1+1*\zeta) + \frac{2}{3}\frac{\zeta - 14.28}{exp(c)} + 8.525\right] \tag{A.33}$$

and

$$\psi_t = \psi_q = -\left[(1+1*\zeta)^{1.5} + \frac{2}{3}\frac{\zeta - 14.28}{exp(c)} + 8.525\right] \tag{A.34}$$

where $c = min(50, 0.35\zeta)$.

The momentum roughness length is given by:

$$z_0 = a_1 \frac{u_*^2}{g} + a_2 \frac{\nu}{u_*} \tag{A.35}$$

where, Charnock's constant, a_1 is given as $a_1 = 0.0017 u_{10N} - 0.005$ the roughness length of humidity and temperature are given as:

$$z_{0t} = z_{0q} = min(1.6 * 10^{-4}, 5.8 * 10^{-5} * Re^{-0.72}) \tag{A.36}$$

where Re is the Reynolds Number.

A.1.3 ECMWF - IFS

The turbulent fluxes can be expressed, using MOST, in terms of the gradients of wind, dry static energy and specific humidity, which are assumed to be proportional to universal gradient functions of a stability parameter given by A.1, A.2 and A.3. The surface fluxes are expressed in terms of differences between parameters at level z_n and surface quantities. The transfer coefficients are expressed as:

$$C_{(D,E,H)} = \kappa^2 \left[ln\left(\frac{Z_A}{z_{0m}}\right) - \psi_m \right]^{-1} \left[ln\left(\frac{Z_A}{z_{0(m,e,h)}}\right) - \psi_{(m,e,h)} \right]^{-1} \tag{A.37}$$

For unstable conditions, the stability profile functions are given as:

$$\psi_m = \frac{\pi}{2} - 2tan{-}1((1-16\zeta)^{1/4}) + log\frac{(1+(1-16\zeta)^{1/4})^2 * (1+(1-16\zeta)^{1/2})}{8} \tag{A.38}$$

$$\psi_h = \psi_q = 2log\frac{(1+(1-16\zeta)^{1/2})}{2} \tag{A.39}$$

for stable conditions,

$$\psi_m = -b(\zeta - c/d)exp(-d\zeta) - a\zeta - bc/d \tag{A.40}$$

$$\psi_h = \psi_q = -b(\zeta - c/d)exp(-d\zeta) - (1 + 2/3a\zeta)^{1.5} - bc/d + 1 \tag{A.41}$$

where a=1, b = 2/3, c=5 and d=0.35. The momentum roughness length is given by equation A.25 where, a_1 is 0.11 and a_2 is 0.4. The temperature roughness length is given

as:

$$z_{oh} = 0.4\frac{\nu}{u_*} \tag{A.42}$$

The humidity roughness length is given as:

$$z_{oq} = 0.62\frac{\nu}{u_*} \tag{A.43}$$

Appendix B

Experiments

In this chapter we present the laboratory experiments we have done to check if the facilities we have at the University of Melbourne can be used to compute the air-water gas transfer across the interface.

B.1 Momentum Fluxes

Momentum fluxes in the wind wave tank can be computed using various methods, in this study profile method is been used. The experiments are conducted in the Extreme air sea interaction facility whose description is given in the section below.

B.1.1 The Extreme Air-Sea Interaction (EASI) facility

The Extreme Air-Sea Interaction (EASI) facility, situated in Mitchell Hydrodynamics lab at The University of Melbourne is used in our current study to perform the experiments to compute the fluxes across the air-water interface. Figure B.1 shows the schematic of the EASI facility. The flume facility is 1.8 m wide, 60 m long with 38.5 m being exposed to the wind and has a total height of 2 m, of which about 0.9 m is filled with water. Computer controlled mechanical and wind waves are generated to study the waves and air-sea interactions. The winds in the facility are generated by a 280 kW counter rotating fan pair which produces maximum wind speeds of about 35 m/s. A honeycomb structure, a stainless steel mesh and a contractor unit are provided at the entrance of the wind

tunnel flume for flow straightening and to reduce the turbulence. A mechanical wave generator is located at the starting end of the tank, while a sloped beach and diffuser is provided at the other end of the flume to reduce the wave energy and minimize the wave reflections and decrease the velocity of the air that exits the flume. The facility has see through windows to allow optical measurements at a fetch of 22 m. The total water volume of the tank is 97.2 m^3, the total surface area of still water exposed to air is 69.3 m^2 and the total volume of the air is 955 m^3.

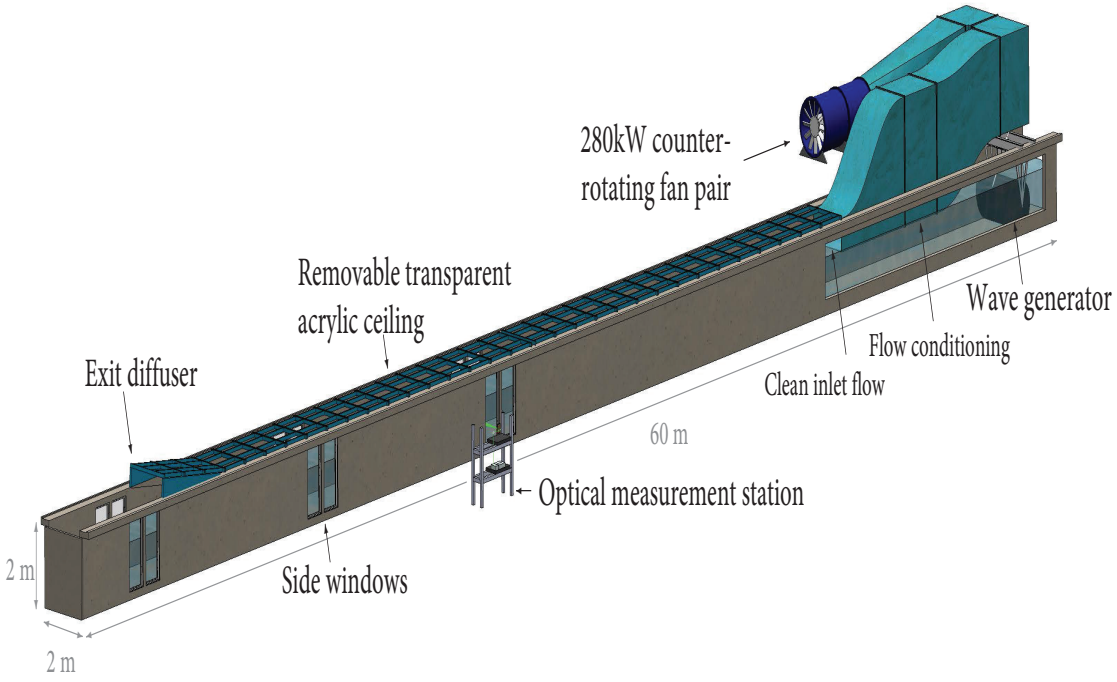

FIGURE B.1: *Schematic of the EASI Facility located in Mitchell Hydrodynamics Laboratory, The University of Melbourne. Adapted from Lee (2019)*

B.1.2 Velocity Profiles

The turbulent boundary layers in the aerodynamic tubes and wind flumes have three different sublayers at different distances from the surface of the water, the viscous sublayer, layer of constant fluxes and the wake. The viscous sublayer is the layer where viscous effects are essential and is typically about 1 mm. The layer of constant fluxes is the only layer that has a logarithmic velocity profile and the can be extrapolated to the meteorological height H_{10}. The wake is the outer part of the turbulent boundary layer, where the boundary layer flow transits into the outer flow in the tube. Typically in the

aerodynamic tubes, the layer of constant fluxes extends from the upper boundary of the viscous layer to approximately 0.15 times the boundary layer thickness.

Experiments are conducted in the EASI facility to verify that the wind wave tank can be used to compute the momentum transfer at the surface. The aerodynamic resistance at the air-water interface is calculated by using the logarithmic fit to the measured velocity profiles in the flume at a fetch distance of 21 m. Wind velocity profiles are measured by the L-shaped Pitot tube with differential Baratron MKS pressure transducer. The lowest measurement point was chosen such that it was very close to the crest of the waves, which depended on the wind speed. The distance from the surface and the lowest point of measurement was obtained using the pixel distance that is calibrated to real space. The measurements were made with logarithmic height increments with a sampling time of 10 minutes at each point to obtain convergence. The velocity profile in the layer of constant fluxes is given by equation (1.6). Figure B.2 shows the wind profiles measured over the waves in the aerodynamic flume. The solid lines indicate the logarithmic approximation of the in the constant flux layer. The friction velocity and roughness length z_0 are calculated by using a logarithmic fit to the wind profile and the wind speed at meteorological height, 10 m is obtained by extrapolating the fit. Figure B.4 shows the friction velocity as a function of wind speed.

B.2 Heat Fluxes as a proxy

B.2.1 Integral Conservation method

The integral conservation method or calorimetric method is described by Jeong et al. (2012) is used in this study to calculate enthalpy flux. In this method, the enthalpy flux across the interface is calculated based on the heat lost by the water as air is blown over the surface. The total moist enthalpy flux is given by

$$H_K = -c_{p_l}\rho_l \frac{\partial T_W}{\partial t}\frac{V_W}{A} \tag{B.1}$$

where c_{p_l} is the specific heat capacity of liquid water ($4.181\,\mathrm{kJ}kg^{-1}K^{-1}$ at 25^o C), ρ_l is the density of water ($997\,kgm^{-3}$ at 25^oC), $\frac{\partial T_W}{\partial t}$ is the rate of change of the bulk

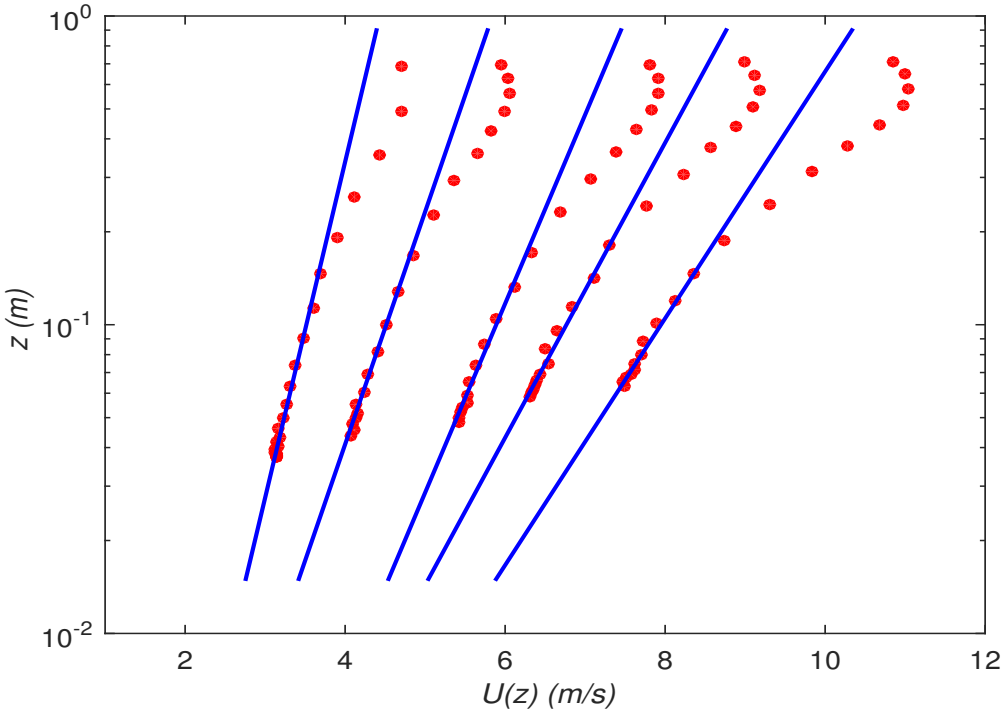

FIGURE B.2: *Wind profiles in the aerodynamic flume over the waves for different inlet winds; the solid line is the logarithmic approximation in the layer of constant fluxes.*

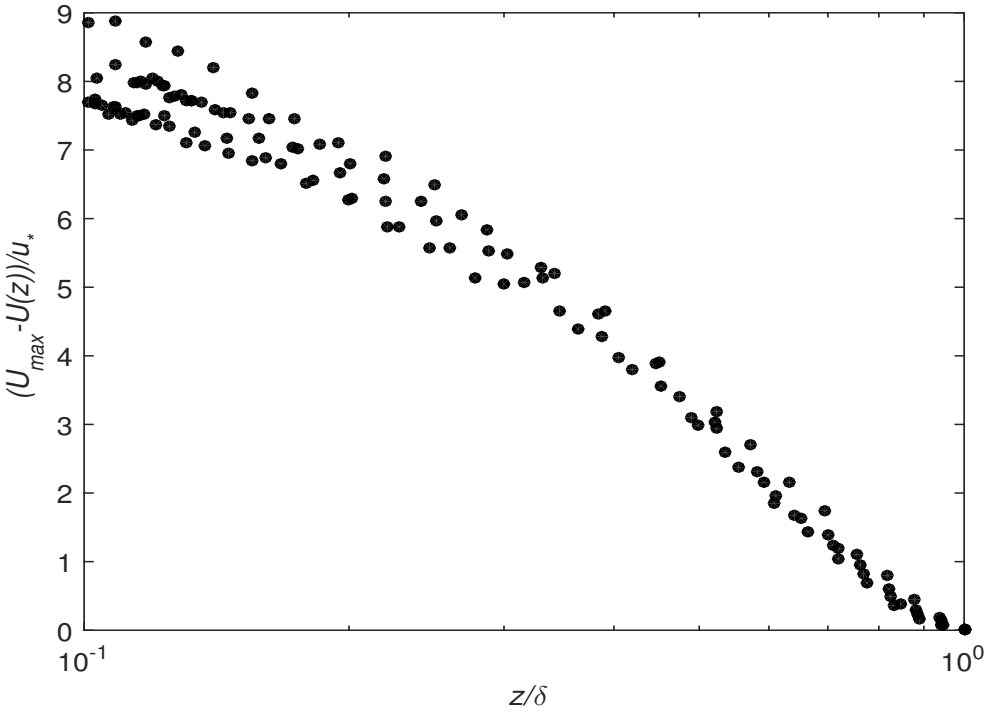

FIGURE B.3: *Wind profiles in the aerodynamic flume measured for different inlet winds over the waves in terms of self-similar variables.*

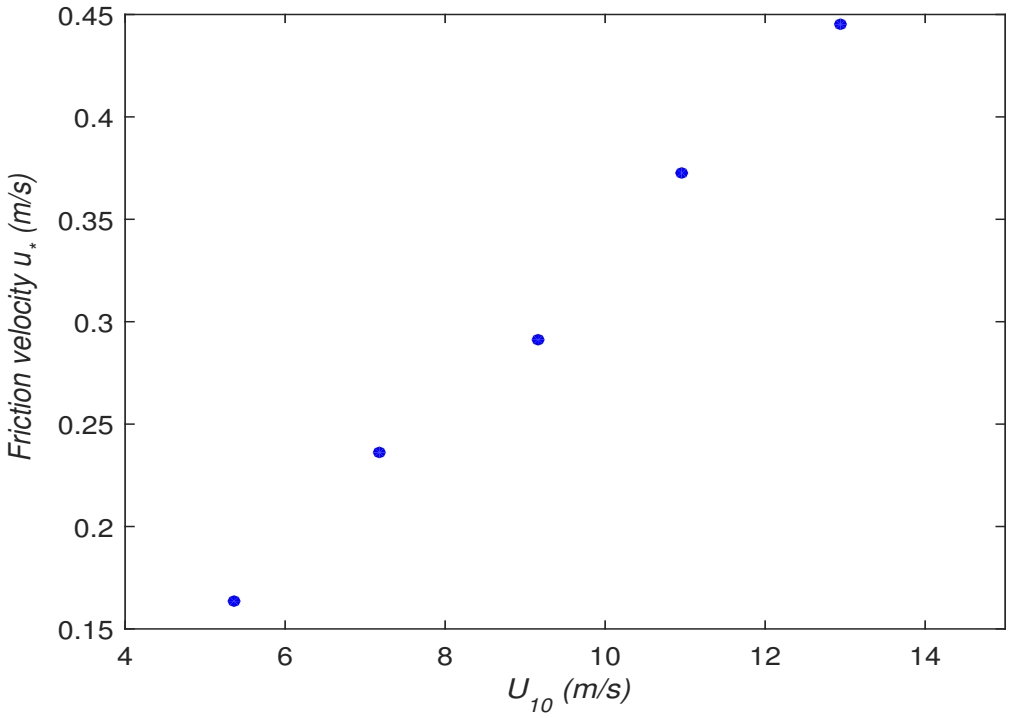

FIGURE B.4: *Air friction velocity u_* as a function of wind speed.*

water temperature, V_W is the total volume of water and A is the area of the air-water interface exposed to the wind. The total heat loss is due to the sensible heat flux, latent heat flux at the interface, flux due to spray, conduction and radiation heat flux at the wall surface. The sensible heat flux is the heat exchanged by the bodies with different temperatures. At the interface, heat flux from the warmer to the cooler surface takes place till both the media reach the same temperatures. Latent heat flux is due to phase transformation. Two common forms of latent heat are latent heat of fusion (solid to liquid) and latent heat of vaporization (liquid to gas). If thermal gradients exist at the walls of the wind wave tank, the heat loss may be due to conduction and radiation. If the conduction and radiative heat losses are known, the moist enthalpy fluxes due to interfacial fluxes and spray can be known by

$$H_K = -c_{pl}\rho_l \frac{V_W}{A}\left(\frac{\partial T_W}{\partial t} - \frac{\partial T_{WC}}{\partial t}\right) \tag{B.2}$$

where $\frac{\partial T_{WC}}{\partial t}$ represents the conduction and radiation induced cooling rate through the side walls of the wind wave tank. The temperature decrease in the water is due to sensible and latent heat losses through the interface, conductive and radiation losses

through the walls of wind wave tank and the sensible heat transferred by the re-entrant spray. The 10-m neutral enthalpy exchange coefficients (C_{K10N}) are calculated by:

$$C_{K10N} = \frac{H_K}{\rho U_{10N}(e_s - e_{10N})} \tag{B.3}$$

where subscripts s and $10N$ denotes measurements at surface and at 10 m above the surface in neutral conditions, $e = (1-q)c_pT + q(L_v + c_{p_v}T)$ is the specific moist enthalpy, L_v is the latent heat of vaporization of water, t is the temperature, c_{p_v} is the specific heat of water vapor and q is the specific humidity (defined as the ratio of mass of water vapor to the total mass of moist air parcel).

B.2.2 Instrumentation and setup

Temperature and specific humidity are measured during each experiment to calculate enthalpy flux using the calorimetric method described by Jeong et al. (2012). The mean temperatures of air and water are taken at two different fetches of 6 m and 25.1 m. The air temperatures are measured at 25 cm above the water surface and water temperatures are measured at 15 cm below the surface of water. The specific humidity is obtained through absolute water content measured by Picarro Gas Analyzer at a fetch of 16 m. Gas Analyzer works on the principle of cavity ring down spectroscopy that gives the absolute water content and is converted to specific humidity by multiplying with the ratio of molecular weights of water and air. The saturated value for specific humidity is estimated from the average of the last portion of the record from the gas analyzer. Omega thermistors with an operating range between -18°C and 150°C and tolerance of ± 0.2 are used to measure the temperatures of air and water. Picarro CRDS instrument is used to measure the specific humidity with an operating range between 0-7% v of H_2O and precision of 30ppm averaged over 5min.

B.2.2.1 Cavity Ring Down Spectroscopy (CRDS)

Spectroscopy is a study of the interaction of light and matter. CRDS measures the concentration of constituents of the gas sample by measuring the decay rate of a laser induced into a cavity formed by two or more mirrors of known reflectivity and transmission. The decay of transmitted power is exponential with time. Picarro Analyzer uses

a three mirror cavity of length 25 cm. A photodetector is used to get the cavity decay rate, which is inversely proportional to losses in the cavity. For an empty cavity, total losses depend only on reflectivity and the decay time is longer for high reflective mirrors. When a gas is introduced into the cavity, a second loss due to absorption is introduced and the decay time decreases, this change in decay time with and without absorbers is used to calculate the concentration of gases in the cavity (Berden and Engeln (2009)).

Experiments were run in the EASI facility to calculate moist enthalpy flux using calorimetric method of Jeong et al. (2012) and to calculate water vapor transfer velocity by the method followed by Ocampo-Torres et al. (1994). Experiments produce a time series of air and water temperature data at two different stations and the % volume of H_2O in air. The temperature fluctuations at station 2 are more as the turbulence is high. The turbulent moist enthalpy flux is calculated by using Equation B.2. In our experiments the air-water temperature difference is less than 2^o, we assume the sensible heat fluxes through the walls of the tank as negligible. $\frac{\partial T_W}{\partial t}$ is the total heat lost by the bulk water due to the interfacial fluxes. This is achieved by a polynomial fit of sixth order to the bulk water temperature.

The water vapor transfer velocity can be calculated by using

$$\frac{\partial Q}{\partial t}\frac{V_a}{A} = k_{H_2O}(Q_s - Q) \tag{B.4}$$

The time series data of specific humidity in air calculated from % volume of H_2O given by gas analyzer is shown in Figure B.5. The data from gas analyzer is at a frequency of 0.2 Hz. Figure B.6 shows a scatter plot of $\partial Q/\partial t$ with $Q_s - Q$. The transfer velocity is slope of the fitted straight line. Summary of experiments conducted to calculate enthalpy flux (H_K) and transfer velocity of water vapor (k_{H_2O}) are presented in Table B.1.

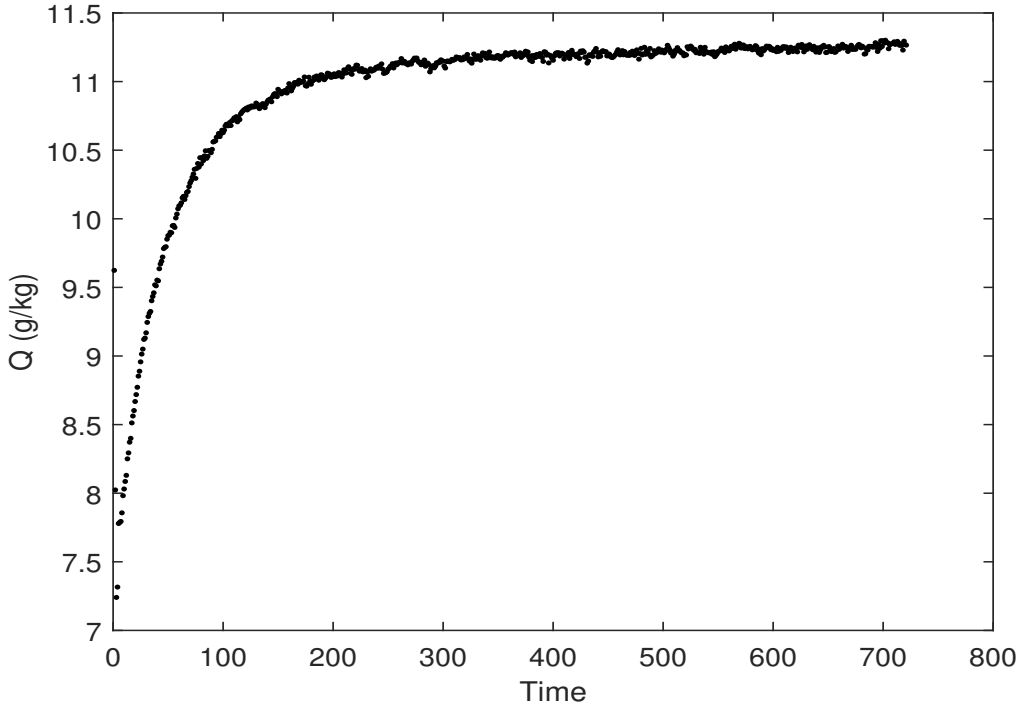

FIGURE B.5: *Specific humidity calculated from water content from gas analyzer.*

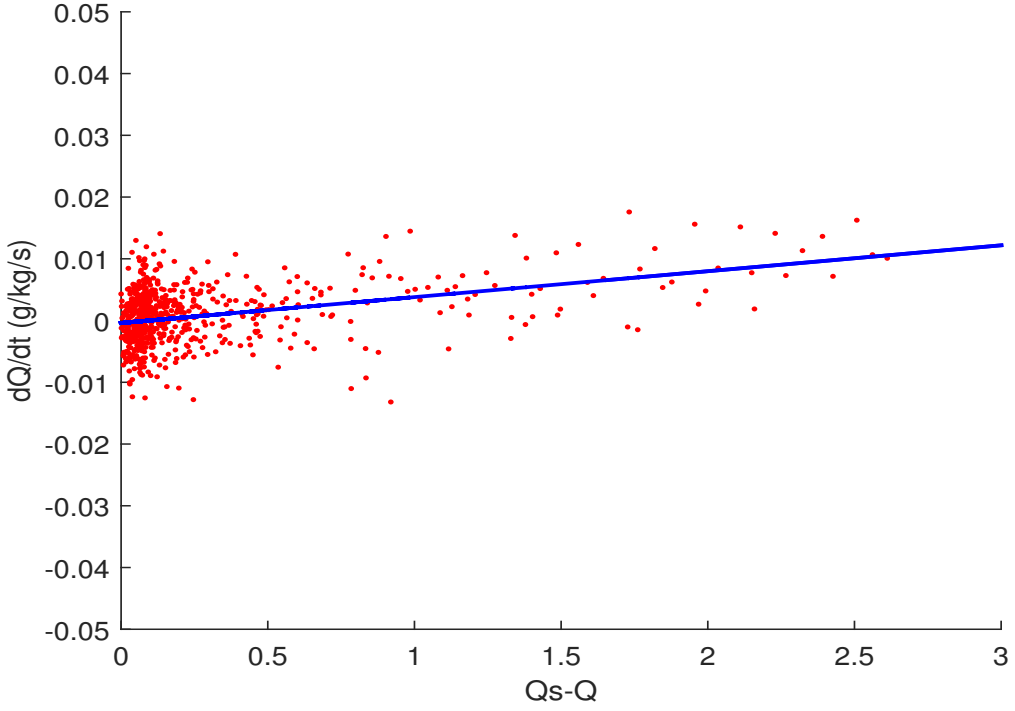

FIGURE B.6: *Scatter plot of $\partial Q/\partial t$ versus $Q_s - Q$. The slope of the fitted solid line is the mass transfer velocity of the water vapor.*

Run	**Time** (s)	$\mathbf{T}_a$ (°C)	$\mathbf{T}_w$(°C)	**U** (m/s)	$\mathbf{k}_{H_2O}$ (m/s)	$\mathbf{H}_K$ (W/m^2)
1	3600	19.263	18.767	3.132	0.000378	11.7126
2	3600	18.959	18.693	4.270	-	7.7214
3	3600	20.957	18.644	5.287	0.000789	7.5357
4	3600	20.446	18.783	6.323	0.0010	8.5083
5	3600	21.337	18.794	7.296	0.0014	15.0112
6	3600	20.97	18.919	8.2752	0.0016	14.5320

TABLE B.1: Summary of Experiments.

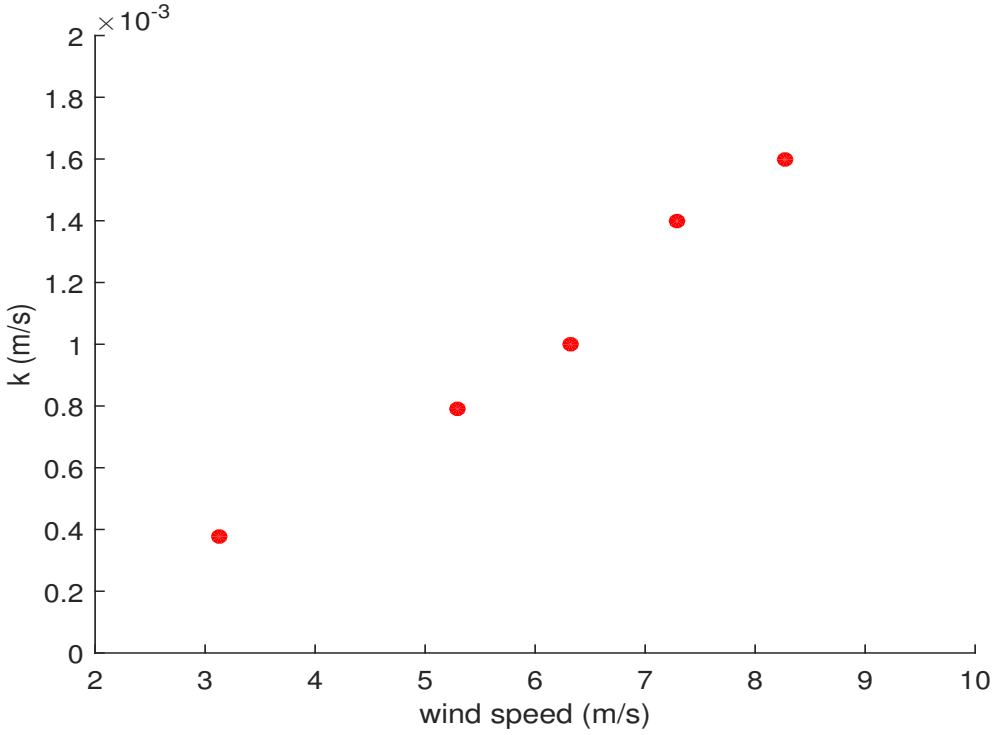

FIGURE B.7: *Mass transfer velocity of H_2O versus wind speed within the EASI facility.*

Figure B.7 shows the mass transfer velocity of H_2O versus reference wind speed within the EASI facility. Ocampo-Torres et al. (1994) measured water vapor transfer velocity

in a Gas Transfer Flume (32.2 m × 0.76 m × 0.85 m). The observed transfer velocities are in the range of 0.002 m/s to 0.0499 m/s for wind speeds between 1 m/s to 15 m/s. The transfer velocities obtained in our experimental results are between 0.000343 and 0.0017 for velocities ranging from 3 m/s to 8 m/s which are less when compared to that obtained by Ocampo-Torres et al. (1994). This can be due to leaks in the experimental setup. It is observed that the wind speeds at exit of flume is nearly half of that observed at entry of flume. This shows that there are leaks through the acrylic ceiling. It is also observed there are few leaks to the surrounding atmosphere through the recirculating area which has to be fixed before continuing further experiments.

B.2.3 Leak Rate

The leak rate (λ) can be defined as the ratio of amount of air replaced in a given time to the total ($\dot{V_a}$) volume (V_a). For mass balance method ideally we need to have a leak rate equal to zero, but it in reality it is hard to achieve. The major leak to the system is found at the downstream of the tank and the volume flow rate at the leak is calculated. The leak rates are found to be between $2.3*10^{-4}\,\mathrm{sec}^{-1}$ and $1.15*10^{-5}\,\mathrm{sec}^{-1}$. If we consider the air side control volume and removing the exchange terms across the interface, Equation **??** becomes

$$V_a \dot{c_a} = \dot{V_a}(c_a^i - c_a) \tag{B.5}$$

which can be rewritten as

$$\dot{c_a} = \lambda(c_a^i - c_a) \tag{B.6}$$

The solution to the above equation is

$$c = c_a^i + (c_{a0} - c_a^i)e^{-\lambda t} \tag{B.7}$$

Figure B.8 shows the concentration time series for a system with different leak rates when initial concentration is increased to 900 ppm and with a background concentration of 450 ppm. With these leak rates, as we increase the air side concentrations to 900 ppm there will not be significant change in the water side concentrations. In order to conduct the air sea gas transfer experiments with air side concentrations to only 1000 ppm, the leak rate has to be reduced. Leak rates reduction for the EASI facility is pretty hard

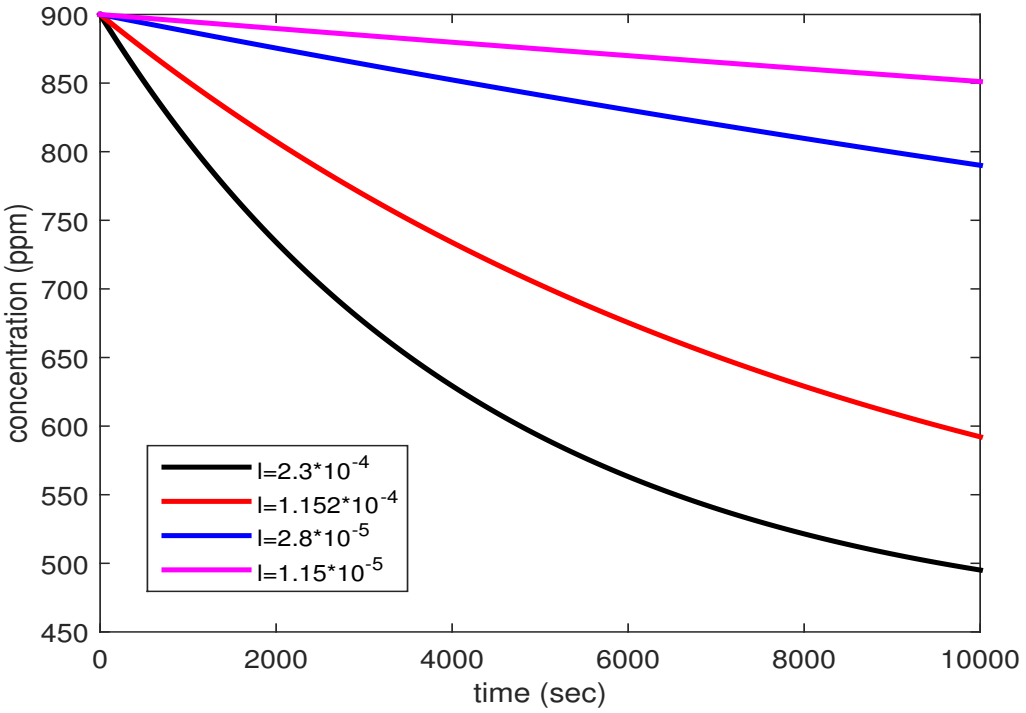

FIGURE B.8: *Air side concentration time series with different leak rates.*

due to the size and built of the facility, so a relatively small Sea-Ice Wind Wave Wave Interaction Facility is used for further experiments. A brief description of the facility is given in the following subsection.

B.3 CO_2 Fluxes

B.3.1 The Sea-Ice Wind Wave Interaction (SIWWI) Facility

The Sea-Ice Wind Wave Interaction (SIWWI) Facility, situated in Mitchell Hydrodynamics lab of the University of Melbourne is used to check if we can calculate the carbon dioxide fluxes at high wind speeds as we have deduced that EASI facility can not be used due to the fact that it has higher leak rates. SIWWI facility is a 14 m long, 0.75 m wide and 0.7 m height tank with water filled up to 0.35 m and a fetch of 6.6 m exposed to wind. There is wave maker at the starting to generate mechanical waves and there is a beach made of woven Nylon placed at end of the tank at 7° to minimize the reflections of the waves. A honeycomb structure and a stainless steel mesh are placed for flow straightening. A counter rotating fan is used to produce the winds. The operating range

of the fan is between 17 Hz and 33 Hz. The total volume of water is 3.675 m^3 and surface area exposed to air is 4.95 m^2. The whole wind wave setup is inside a freezer room built from 100 mm thick foam refrigeration panels with two heated, double glazed windows. The temperature of the room can be controlled between ambient and -12°C using three 5 kW evaporator units. Figure B.9 shows a 3D diagram of the SIWWI facility.

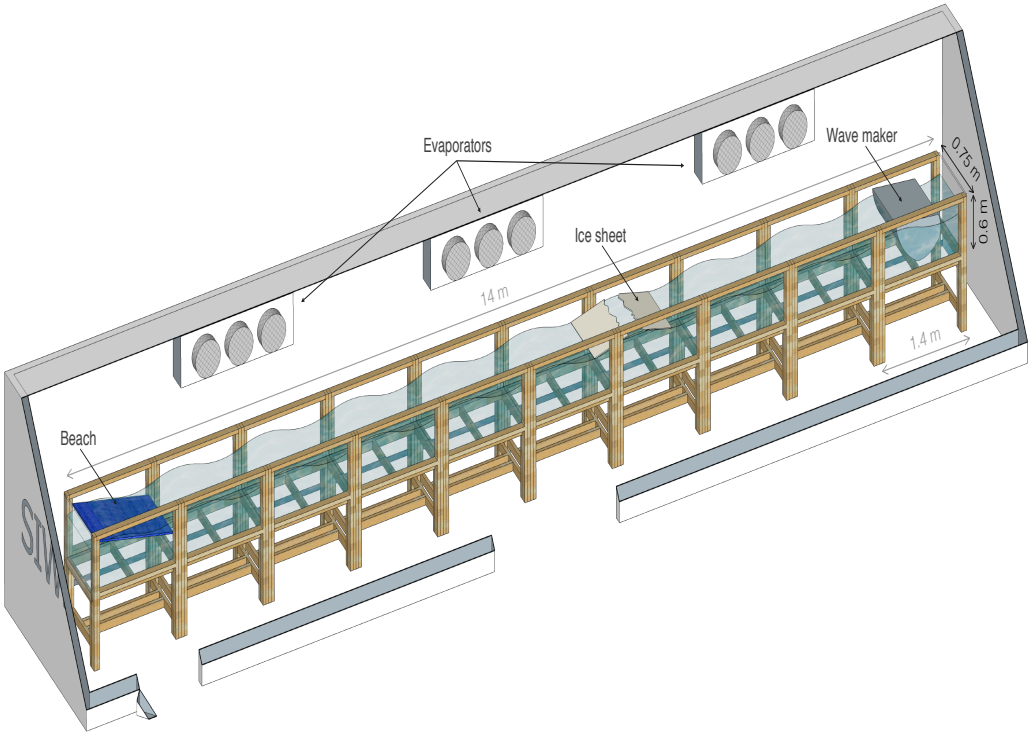

FIGURE B.9: *Schematic of the SIWWI Facility.*

B.3.2 Measurement of Total Inorganic Carbon in water

The total Dissolved Inorganic Carbon (DIC) measured is a combination of carbonates and carbon dioxide dissolved in water. DIC measurements are to be done using total organic carbon (TOC) measuring instrument, SHIMADZU TOC-V_{CSH} in which DIC is measured by acidifying the sample with small amount of Hydrochloric acid to obtain a pH less than 3, where all carbonates are converted to carbon dioxide and this sample is volatilized through bubbling with Nitrogen gas and the carbon dioxide in the gas sample is detected using NDIR. Figure B.10 shows the schematic of the DIC measurements using TOC. The concentration in the sample is obtained through comparison with a calibration curve equation. Figure B.11 shows a multi-point calibration curve for different known concentrations.

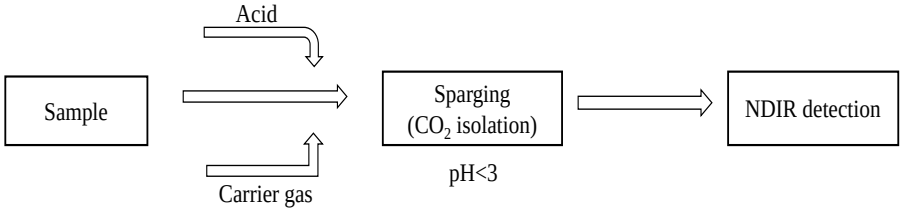

FIGURE B.10: *Schematic diagram of DIC measurements using TOC.*

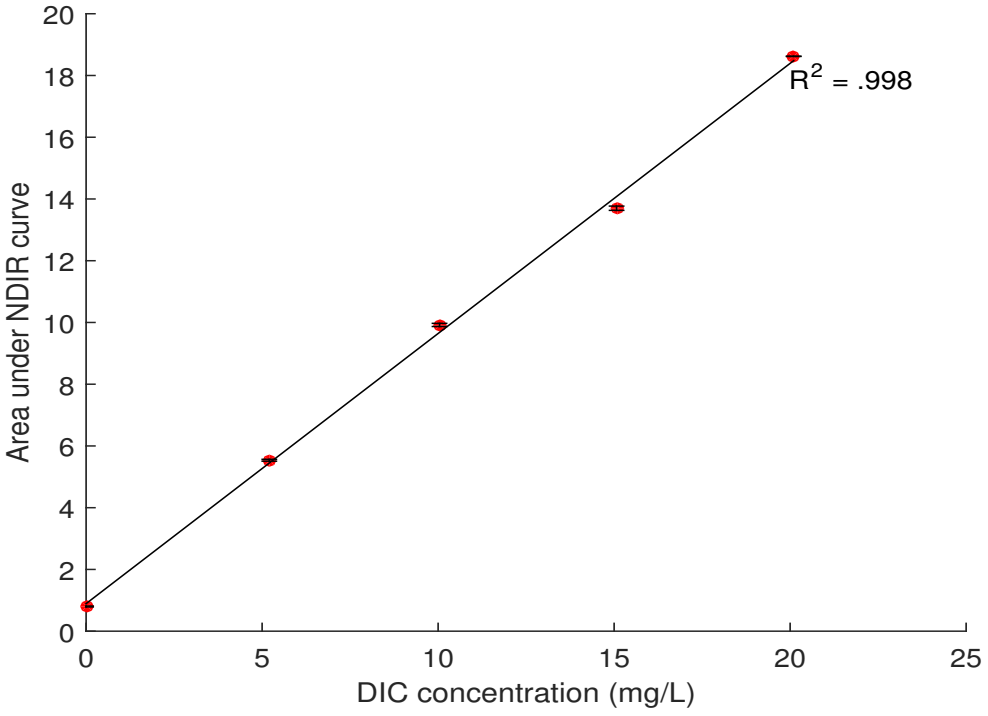

FIGURE B.11: *Calibration curve for DIC measurements.*

B.3.3 Measurements of carbon dioxide in air

Picarro CRDS instrument is used to measure the air side concentration of carbon dioxide. A brief description of the instrument is given in the section B.2.2.1. To determine the leaks in the SIWWI system, continuous measurements of carbon dioxide with no water and doors of the system closed were done. It is found that the carbon dioxide concentration in the system is was continuously being raised with in the system, while the gradients of the rise in concentration varied with the temperature with in the system and the air circulation speed. After a careful observation, it is found that the carbon dioxide is released into the system through the cracks on the floor. Hence, the cracks are to be sealed to further continue the experiments.

Bibliography

Andreas, E. L., Mahrt, L., and Vickers, D. (2012). A new drag relation for aerodynamically rough flow over the ocean. *Journal of the Atmospheric Sciences*, 69(8):2520–2537.

Asher, W. and Wanninkhof, R. (1998). Transient tracers and air-sea gas transfer. *Journal of Geophysical Research: Oceans*, 103(C8):15939–15958.

Asher, W. E., Karle, L. M., Higgins, B. J., Farley, P. J., Monahan, E. C., and Leifer, I. S. (1996). The influence of bubble plumes on air-seawater gas transfer velocities. *Journal of Geophysical Research: Oceans*, 101(C5):12027–12041.

Aubinet, M., Vesala, T., and Papale, D. (2012). *Eddy covariance: a practical guide to measurement and data analysis*. Springer Science & Business Media.

Bariteau, L., Fairall, C. W., Blomquist, B. W., and Pezoa, S. (2018). CAPRICORN 2016 field campaign: Surface meteorological data and turbulent fluxes collected from the RV Investigator by the National Oceanographic and Atmospheric Administration (NOAA) in the Indian and South Pacific Oceans from 2016-03-14 to 2016-04-15. NOAA/National Centers for Environmental Information.

Berden, G. and Engeln, R. (2009). *Cavity ring-down spectroscopy: techniques and applications*. John Wiley & Sons.

Bharti, V., Fairall, C. W., Blomquist, B. W., Huang, Y., Protat, A., Sullivan, P. P., Siems, S. T., and Manton, M. J. (2019). Air-sea heat and momentum fluxes in the Southern Ocean. *Journal of Geophysical Research: Atmospheres*.

Blomquist, B. W., Brumer, S. E., Fairall, C. W., Huebert, B. J., Zappa, C. J., Brooks, I. M., Yang, M., Bariteau, L., Prytherch, J., Hare, J. E., et al. (2017). Wind speed and sea state dependencies of air-sea gas transfer: Results from the high wind speed gas

exchange study (HiWinGS). *Journal of Geophysical Research: Oceans*, 122(10):8034–8062.

Blomquist, B. W., Fairall, C. W., Huebert, B. J., Kieber, D. J., and Westby, G. R. (2006). DMS sea-air transfer velocity: Direct measurements by eddy covariance and parameterization based on the NOAA/COARE gas transfer model. *Geophysical Research Letters*, 33(7).

Bumke, K., Schlundt, M., Kalisch, J., Macke, A., and Kleta, H. (2014). Measured and parameterized energy fluxes estimated for Atlantic transects of R/V Polarstern. *Journal of Physical Oceanography*, 44(2):482–491.

Businger, J. A., Wyngaard, J. C., Izumi, Y., and Bradley, E. F. (1971). Flux-profile relationships in the atmospheric surface layer. *Journal of the atmospheric Sciences*, 28(2):181–189.

Butterworth, B. J. and Miller, S. D. (2016). Air-sea exchange of carbon dioxide in the southern ocean and antarctic marginal ice zone. *Geophysical Research Letters*, 43(13):7223–7230.

Carpenter, L. J., Archer, S. D., and Beale, R. (2012). Ocean-atmosphere trace gas exchange. *Chemical Society Reviews*, 41(19):6473–6506.

Charnock, H. (1955). Wind stress on a water surface. *Quarterly Journal of the Royal Meteorological Society*, 81(350):639–640.

Cook, P. A. and Renfrew, I. A. (2015). Aircraft-based observations of air–sea turbulent fluxes around the British Isles. *Quarterly Journal of the Royal Meteorological Society*, 141(686):139–152.

Crosswell, J. R. (2015). Bubble Clouds in Coastal Waters and Their Role in Air-Water Gas Exchange of CO_2. *Journal of Marine Science and Engineering*, 3(3):866–890.

Csanady, G. T. (2001). *Air-sea interaction: laws and mechanisms*. Cambridge University Press.

DeCosmo, J., Katsaros, K. B., Smith, S. D., Anderson, R. J., Oost, W. A., Bumke, K., and Chadwick, H. (1996). Air-sea exchange of water vapor and sensible heat: The Humidity Exchange Over the Sea (HEXOS) results. *Journal of Geophysical Research: Oceans*, 101(C5):12001–12016.

Dee, D. P., Uppala, S. M., Simmons, A. J., Berrisford, P., Poli, P., Kobayashi, S., Andrae, U., Balmaseda, M. A., Balsamo, G., Bauer, P., Bechtold, P., Beljaars, A. C. M., van de Berg, L., Bidlot, J., Bormann, N., Delsol, C., Dragani, R., Fuentes, M., Geer, A. J., Haimberger, L., Healy, S. B., Hersbach, H., Hlm, E. V., Isaksen, L., Kllberg, P., Khler, M., Matricardi, M., McNally, A. P., Monge-Sanz, B. M., Morcrette, J.-J., Park, B.-K., Peubey, C., de Rosnay, P., Tavolato, C., Thpaut, J.-N., and Vitart, F. (2011). The ERA-Interim reanalysis: configuration and performance of the data assimilation system. *Quarterly Journal of the Royal Meteorological Society*, 137(656):553–597.

Donelan, M. A. (2018). On the decrease of the oceanic drag coefficient in high winds. *Journal of Geophysical Research: Oceans*, 123(2):1485–1501.

Donelan, M. A., Curcic, M., Chen, S. S., and Magnusson, A. K. (2012). Modeling waves and wind stress. *Journal of Geophysical Research: Oceans*, 117(C11).

Donelan, M. A., Haus, B. K., Reul, N., Plant, W. J., Stiassnie, M., Graber, H. C., Brown, O. B., and Saltzman, E. S. (2004). On the limiting aerodynamic roughness of the ocean in very strong winds. *Geophysical Research Letters*, 31(18).

Drennan, W. M., Zhang, J. A., French, J. R., McCormick, C., and Black, P. G. (2007). Turbulent fluxes in the hurricane boundary layer. Part II: Latent heat flux. *Journal of the atmospheric sciences*, 64(4):1103–1115.

Edson, J. B., Fairall, C. W., Bariteau, L., Zappa, C. J., Cifuentes-Lorenzen, A., McGillis, W. R., Pezoa, S., Hare, J. E., and Helmig, D. (2011). Direct covariance measurement of CO_2 gas transfer velocity during the 2008 Southern Ocean Gas Exchange Experiment: Wind speed dependency. *Journal of Geophysical Research: Oceans*, 116(C4).

Edson, J. B., Hinton, A. A., Prada, K. E., Hare, J. E., and Fairall, C. W. (1998). Direct covariance flux estimates from mobile platforms at sea. *Journal of Atmospheric and Oceanic Technology*, 15(2):547–562.

Edson, J. B., Jampana, V., Weller, R. A., Bigorre, S. P., Plueddemann, A. J., Fairall, C. W., Miller, S. D., Mahrt, L., Vickers, D., and Hersbach, H. (2013). On the exchange of momentum over the open ocean. *Journal of Physical Oceanography*, 43(8):1589–1610.

Fairall, C. W., Bradley, E. F., Hare, J. E., Grachev, A. A., and Edson, J. B. (2003). Bulk parameterization of air–sea fluxes: Updates and verification for the COARE algorithm. *Journal of climate*, 16(4):571–591.

Frew, N. M., Bock, E. J., Schimpf, U., Hara, T., Haußecker, H., Edson, J. B., McGillis, W. R., Nelson, R. K., McKenna, S. P., Uz, B. M., et al. (2004). Air-sea gas transfer: Its dependence on wind stress, small-scale roughness, and surface films. *Journal of Geophysical Research: Oceans*, 109(C8).

Garbe, C. S., Rutgersson, A., Boutin, J., De Leeuw, G., Delille, B., Fairall, C. W., Gruber, N., Hare, J., Ho, D. T., Johnson, M. T., et al. (2014). Transfer across the air-sea interface. In *Ocean-Atmosphere Interactions of Gases and Particles*, pages 55–112. Springer.

Garratt, J. R. (1977). Review of drag coefficients over oceans and continents. *Monthly weather review*, 105(7):915–929.

Geernaert, G. L., Katsaros, K. B., and Richter, K. (1986). Variation of the drag coefficient and its dependence on sea state. *Journal of Geophysical Research: Oceans*, 91(C6):7667–7679.

Ho, D. T., Law, C. S., Smith, M. J., Schlosser, P., Harvey, M., and Hill, P. (2006). Measurements of air-sea gas exchange at high wind speeds in the Southern Ocean: Implications for global parameterizations. *Geophysical Research Letters*, 33(16).

Högström, U. (1996). Review of some basic characteristics of the atmospheric surface layer. *Boundary-Layer Meteorology*, 78(3-4):215–246.

Högström, U., Bergström, H., Smedman, A., Halldin, S., and Lindroth, A. (1989). Turbulent exchange above a pine forest, I: Fluxes and gradients. *Boundary-Layer Meteorology*, 49(1-2):197–217.

Holthuijsen, L. H., Powell, M. D., and Pietrzak, J. D. (2012). Wind and waves in extreme hurricanes. *Journal of Geophysical Research: Oceans*, 117(C9).

Hwang, P. A., Hsu, Y. L., and Wu, J. (1990). Air bubbles produced by breaking wind waves: A laboratory study. *Journal of Physical Oceanography*, 20(1):19–28.

Iwano, K., Takagaki, N., Kurose, R., and Komori, S. (2013). Mass transfer velocity across the breaking air-water interface at extremely high wind speeds. *Tellus B*, 65.

Jackson, D. L., Wick, G. A., and Hare, J. E. (2012). A comparison of satellite-derived carbon dioxide transfer velocities from a physically based model with GasEx cruise observations. *Journal of Geophysical Research: Oceans*, 117(C4).

Jähne, B. and Haußecker, H. (1998). Air-water gas exchange. *Annual Review of Fluid Mechanics*, 30(1):443–468.

Jarosz, E., Mitchell, D. A., Wang, D. W., and Teague, W. J. (2007). Bottom-up determination of air-sea momentum exchange under a major tropical cyclone. *Science*, 315(5819):1707–1709.

Jeong, D., Haus, B. K., and Donelan, M. A. (2012). Enthalpy transfer across the air–water interface in high winds including spray. *Journal of the Atmospheric Sciences*, 69(9):2733–2748.

Kara, A. B., Hurlburt, H. E., and Wallcraft, A. J. (2005). Stability-dependent exchange coefficients for air–sea fluxes. *Journal of Atmospheric and Oceanic Technology*, 22(7):1080–1094.

Komori, S., Takagaki, N., Saiki, R., Suzuki, N., and Tanno, K. (2007). The effect of raindrops on interfacial turbulence and air-water gas transfer. In *Transport at the Air-Sea Interface*, pages 169–179. Springer.

Krall, K. E. and Jähne, B. (2014). First laboratory study of air-sea gas exchange at hurricane wind speeds. *Ocean Science*, 10(2):257.

Landwehr, S., Miller, S. D., Smith, M. J., Bell, T. G., Saltzman, E. S., and Ward, B. (2018). Using eddy covariance to measure the dependence of air-sea CO_2 exchange rate on friction velocity. *Atmospheric Chemistry and Physics*, 18(6):4297–4315.

Landwehr, S., Miller, S. D., Smith, M. J., Saltzman, E. S., and Ward, B. (2014). Analysis of the PKT correction for direct CO_2 flux measurements over the ocean. *Atmos. Chem. Phys.*, 14(7):3361–3372.

Large, W. G. and Pond, S. (1981). Open ocean momentum flux measurements in moderate to strong winds. *Journal of physical oceanography*, 11(3):324–336.

Large, W. G. and Pond, S. (1982). Sensible and latent heat flux measurements over the ocean. *Journal of physical Oceanography*, 12(5):464–482.

Liss, P. S., Johnson, M. T., et al. (2014). *Ocean-atmosphere interactions of gases and particles*. Springer.

Liss, P. S. and Merlivat, L. (1986). Air-sea gas exchange rates: Introduction and synthesis. In *The role of air-sea exchange in geochemical cycling*, pages 113–127. Springer.

Mace, G. G. and Protat, A. (2018). Clouds over the Southern Ocean as observed from the R/V Investigator during CAPRICORN. Part I: Cloud occurrence and phase partitioning. *Journal of Applied Meteorology and Climatology*, 57(8):1783–1803.

Matson, P. A. and Harriss, R. C. (2009). *Biogenic trace gases: measuring emissions from soil and water*. John Wiley & Sons.

McGillis, W. R., Edson, J. B., Hare, J. E., and Fairall, C. W. (2001). Direct covariance air-sea CO_2 fluxes. *Journal of Geophysical Research: Oceans*, 106(C8):16729–16745.

McGillis, W. R., Edson, J. B., Zappa, C. J., Ware, J. D., McKenna, S. P., Terray, E. A., Hare, J. E., Fairall, C. W., Drennan, W., Donelan, M., et al. (2004). Air-sea CO_2 exchange in the equatorial Pacific. *Journal of Geophysical Research: Oceans*, 109(C8).

McNeil, C. and D'Asaro, E. (2007). Parameterization of air–sea gas fluxes at extreme wind speeds. *Journal of Marine Systems*, 66(1):110–121.

Miller, S., Marandino, C., De Bruyn, W., and Saltzman, E. S. (2009). Air-sea gas exchange of CO_2 and DMS in the North Atlantic by eddy covariance. *Geophysical Research Letters*, 36(15).

Moreau, S., Penna, A. D., Llort, J., Patel, R., Langlais, C., Boyd, P. W., Matear, R. J., Phillips, H. E., Trull, T. W., Tilbrook, B., et al. (2017). Eddy-induced carbon transport across the Antarctic Circumpolar Current. *Global Biogeochemical Cycles*, 31(9):1368–1386.

Nightingale, P. D., Liss, P. S., and Schlosser, P. (2000a). Measurements of air-sea gas transfer during an open ocean algal bloom. *Geophysical Research Letters*, 27(14):2117–2120.

Nightingale, P. D., Malin, G., Law, C. S., Watson, A. J., Liss, P. S., Liddicoat, M. I., Boutin, J., and Upstill-Goddard, R. C. (2000b). In situ evaluation of air-sea gas exchange parameterizations using novel conservative and volatile tracers. *Global Biogeochemical Cycles*, 14(1):373–387.

Ocampo-Torres, F. J., Donelan, M. A., Merzi, N., and Jia, F. (1994). Laboratory measurements of mass transfer of carbon dioxide and water vapour for smooth and rough flow conditions. *Tellus B*, 46(1):16–32.

Persson, P. O., Hare, J. E., Fairall, C. W., and Otto, W. D. (2005). Air–sea interaction processes in warm and cold sectors of extratropical cyclonic storms observed during FASTEX. *Quarterly Journal of the Royal Meteorological Society: A journal of the atmospheric sciences, applied meteorology and physical oceanography*, 131(607):877–912.

Petersen, G. N. and Renfrew, I. A. (2009). Aircraft-based observations of air–sea fluxes over Denmark Strait and the Irminger Sea during high wind speed conditions. *Quarterly Journal of the Royal Meteorological Society: A journal of the atmospheric sciences, applied meteorology and physical oceanography*, 135(645):2030–2045.

Pickard, G. L. and Emery, W. J. (1961). *Descriptive physical oceanography: an introduction*.

Powell, M. D., Vickery, P. J., and Reinhold, T. A. (2003). Reduced drag coefficient for high wind speeds in tropical cyclones. *Nature*, 422(6929):279.

Rutgersson, A., Andersson, A., and Sahlée, E. (2016). Air-sea gas transfer for two gases of different solubility (CO_2 and O_2). In *IOP Conference Series: Earth and Environmental Science*, volume 35, page 012010. IOP Publishing.

Salter, M. E., Upstill-Goddard, R. C., Nightingale, P. D., Archer, S. D., Blomquist, B. W., Ho, D. T., Huebert, B., Schlosser, P., and Yang, M. (2011). Impact of an artificial surfactant release on air-sea gas fluxes during Deep Ocean Gas Exchange Experiment II. *Journal of Geophysical Research: Oceans*, 116(C11).

Smith, S. D. (1980). Wind stress and heat flux over the ocean in gale force winds. *Journal of Physical Oceanography*, 10(5):709–726.

Smith, S. D., Anderson, R. J., Oost, W. A., Kraan, C., Maat, N., De Cosmo, J., Katsaros, K. B., Davidson, K. L., Bumke, K., Hasse, L., et al. (1992). Sea surface wind stress and drag coefficients: The HEXOS results. *Boundary-Layer Meteorology*, 60(1-2):109–142.

Stull, R. B. (2012). *An introduction to boundary layer meteorology*, volume 13. Springer Science & Business Media.

Takagaki, N. and Komori, S. (2007). Effects of rainfall on mass transfer across the air-water interface. *Journal of Geophysical Research: Oceans*, 112(C6).

Turk, D., Zappa, C. J., Meinen, C. S., Christian, J. R., Ho, D. T., Dickson, A. G., and McGillis, W. R. (2010). Rain impacts on CO_2 exchange in the western equatorial Pacific Ocean. *Geophysical Research Letters*, 37(23).

Vickers, D., Mahrt, L., and Andreas, E. L. (2015). Formulation of the sea surface friction velocity in terms of the mean wind and bulk stability. *Journal of Applied Meteorology and Climatology*, 54(3):691–703.

Wanninkhof, R. (1992). Relationship between wind speed and gas exchange over the ocean. *Journal of Geophysical Research: Oceans*, 97(C5):7373–7382.

Wanninkhof, R., Asher, W. E., Ho, D. T., Sweeney, C., and McGillis, W. R. (2009). Advances in quantifying air-sea gas exchange and environmental forcing. *Annual Review of Marine Science*, 1:213–244.

Wanninkhof, R. and McGillis, W. R. (1999). A cubic relationship between air-sea CO_2 exchange and wind speed. *Geophysical Research Letters*, 26(13):1889–1892.

Webb, E. K., Pearman, G. I., and Leuning, R. (1980). Correction of flux measurements for density effects due to heat and water vapour transfer. *Quarterly Journal of the Royal Meteorological Society*, 106(447):85–100.

Woolf, D. K. (1993). Bubbles and the air-sea transfer velocity of gases. *Atmosphere-Ocean*, 31(4):517–540.

Wu, J. (1980). Wind-stress coefficients over sea surface near neutral conditionsA revisit. *Journal of Physical Oceanography*, 10(5):727–740.

Yang, M., Blomquist, B. W., and Nightingale, P. D. (2014). Air-sea exchange of methanol and acetone during HiWinGS: Estimation of air phase, water phase gas transfer velocities. *Journal of Geophysical Research: Oceans*, 119(10):7308–7323.

Yelland, M. and Taylor, P. K. (1996). Wind stress measurements from the open ocean. *Journal of Physical Oceanography*, 26(4):541–558.

Zappa, C. J., Asher, W. E., Jessup, A. T., Klinke, J., and Long, S. R. (2004). Microbreaking and the enhancement of air-water transfer velocity. *Journal of Geophysical Research: Oceans*, 109(C8).

Zemmelink, H. J., Dacey, J. H., Hintsa, E. J., McGillis, W. R., Gieskes, W. W., Klaassen, W., de Groot, H. W., and de Baar, H. J. (2004). Fluxes and gas transfer rates of the biogenic trace gas DMS derived from atmospheric gradients. *Journal of Geophysical Research: Oceans*, 109(C8).

Zeng, X., Zhao, M., and Dickinson, R. E. (1998). Intercomparison of bulk aerodynamic algorithms for the computation of sea surface fluxes using TOGA COARE and TAO data. *Journal of Climate*, 11(10):2628–2644.

Zhang, J. A., Black, P. G., French, J. R., and Drennan, W. M. (2008). First direct measurements of enthalpy flux in the hurricane boundary layer: The CBLAST results. *Geophysical Research Letters*, 35(14).

Zhao, D. and Toba, Y. (2001). Dependence of whitecap coverage on wind and wind-wave properties. *Journal of oceanography*, 57(5):603–616.

Zhao, D., Toba, Y., Suzuki, Y., and Komori, S. (2003). Effect of wind waves on air–sea gas exchange: proposal of an overall CO_2 transfer velocity formula as a function of breaking-wave parameter. *Tellus B*, 55(2):478–487.

Zou, Z., Zhao, D., Liu, B., Zhang, J. A., and Huang, J. (2017). Observation-based parameterization of air-sea fluxes in terms of wind speed and atmospheric stability under low-to-moderate wind conditions. *Journal of Geophysical Research: Oceans*, 122(5):4123–4142.